remote sensing

MDPI

Article

Characterizing Tidal Marsh Inundation with Synthetic Aperture Radar, Radiometric Modeling, and In Situ Water Level Observations

Brian T. Lamb [1,2,*], Kyle C. McDonald [1,2,3], Maria A. Tzortziou [1,2,4] and Derek S. Tesser [1,2,5]

[1] Department of Earth and Atmospheric Sciences, City College of New York, City University of New York, New York, NY 10031, USA; kmcdonald2@ccny.cuny.edu (K.C.M.); mtzortziou@ccny.cuny.edu (M.A.T.); derek.tesser@slu.edu (D.S.T.)
[2] Earth and Environmental Sciences Program, The Graduate Center, City University of New York, New York, NY 10016, USA
[3] Jet Propulsion Laboratory, California Institute of Technology, Pasadena, CA 91109, USA
[4] NASA Goddard Space Flight Center, Greenbelt, MD 20771, USA
[5] Department of Earth, Environmental, and Geospatial Sciences, Saint Louis University, St. Louis, MO 63108, USA
* Correspondence: blamb@gradcenter.cuny.edu

Abstract: Tidal marshes play a globally critical role in carbon and hydrologic cycles by sequestering carbon dioxide from the atmosphere and exporting dissolved organic carbon to connected estuaries. These ecosystems provide critical habitat to a variety of fauna and also reduce coastal flood impacts. Accurate characterization of tidal marsh inundation dynamics is crucial for understanding these processes and ecosystem services. In this study, we developed remote sensing-based inundation classifications over a range of tidal stages for marshes of the Mid-Atlantic and Gulf of Mexico regions of the United States. Inundation products were derived from C-band and L-band synthetic aperture radar (SAR) imagery using backscatter thresholding and temporal change detection approaches. Inundation products were validated with in situ water level observations and radiometric modeling. The Michigan Microwave Canopy Scattering (MIMICS) radiometric model was used to simulate radar backscatter response for tidal marshes across a range of vegetation parameterizations and simulated hydrologic states. Our findings demonstrate that inundation classifications based on L-band SAR—developed using backscatter thresholding applied to single-date imagery—were comparable in accuracy to the best performing C-band SAR inundation classifications that required change detection approaches applied to time-series imagery (90.0% vs. 88.8% accuracy, respectively). L-band SAR backscatter threshold inundation products were also compared to polarimetric decompositions from quad-polarimetric Phased Array L-band Synthetic Aperture Radar 2 (PALSAR-2) and L-band Uninhabited Aerial Vehicle Synthetic Aperture Radar (UAVSAR) imagery. Polarimetric decomposition analysis showed a relative shift from volume and single-bounce scattering to double-bounce scattering in response to increasing tidal stage and associated increases in classified inundated area. MIMICS modeling similarly showed a relative shift to double-bounce scattering and a decrease in total backscatter in response to inundation. These findings have relevance to the upcoming NASA-ISRO Synthetic Aperture Radar (NISAR) mission, as threshold-based classifications of wetland inundation dynamics will be employed to verify that NISAR datasets satisfy associated mission science requirements to map wetland inundation with classification accuracies better than 80% at 1 hectare spatial scales.

Academic Editor: Alfonso Vitti

Received: 21 September 2024
Revised: 26 December 2024
Accepted: 4 January 2025
Published: 13 January 2025

Citation: Lamb, B.T.; McDonald, K.C.; Tzortziou, M.A.; Tesser, D.S. Characterizing Tidal Marsh Inundation with Synthetic Aperture Radar, Radiometric Modeling, and In Situ Water Level Observations. *Remote Sens.* **2025**, *17*, 263. https://doi.org/10.3390/rs17020263

Keywords: tidal marsh; inundation; radar; SAR; L-band; C-band; PALSAR; PALSAR-2; UAVSAR; Sentinel-1; MIMICS; NISAR

1. Introduction

The accurate characterization of tidal wetland inundation patterns is of critical importance for understanding coastal hydrology, wetland carbon cycling, and biogeochemistry [1–3]. Tidal marsh–estuary interfaces have been described as hotspots for biogeochemical exchange [4–6]. Previous measurements in the Global Change Research Wetland (GCReW) and Blackwater National Wildlife Refuge (NWR) marsh-estuarine systems have shown that the amount of marsh-exported dissolved organic carbon (DOC) is mediated primarily by differences in tidal height and tidal range rather than seasonal variation in biological processes [7]. Measurements of marsh-exported DOC at the GCReW marsh showed a negative correlation with water depth at low tide ($n = 29$, $r = -0.75$), reflecting the extent to which marsh soil porewater (i.e., shallow groundwater) is exported into tidal creeks—a process that is most rapid during the lowest tides. Since low-low tides are often linked to high-high tides, this relationship also reflects the influence of marsh inundation extent in terms of exchange between surface water and marsh soils. Tidal inundation dynamics are expected to shift in response to sea-level rise (SLR), leading to coastal marshes being more inundated [8–10]. Because of the important role that inundation patterns play in mediating carbon exchange and other biogeochemical processes in coastal ecosystems, and considering shifts in ecosystem function and habitat associated with SLR, it is critical to develop accurate monitoring systems for tidal marshes.

The synoptic observations provided by spaceborne remote sensing platforms are ideal for characterization of highly dynamic and difficult-to-access tidal wetlands. Both optical/infrared (hereafter referred to as optical) and microwave remote sensing have been employed for the study of wetland hydrology and inundation dynamics. Optical sensors effectively detect water's strong absorption features in the near infrared (NIR) and shortwave infrared (SWIR) domains relative to the visible domain which has led to the successful development of several optically-based inundation products [11–15]. However, optical imagery is generally limited to characterization of open water extent and can only assess wetland inundation state when vegetation canopies are sufficiently sparse due to limited signal penetration in the optical domain (350–2500 nm). Time-series observations are also limited to daylight and cloud-free conditions. In contrast, longer wavelength (~5–100 cm) active microwave instruments, including synthetic aperture radar (SAR), transmit signals that can effectively penetrate vegetated canopies and characterize the hydrologic state of the underlying surface and are uninhibited by time of day or cloud cover [16–18]. Many studies have demonstrated the utility of SAR in characterizing wetland inundation state [19–33]. However, studies that have sought to assess tidal marsh inundation patterns with SAR have been limited [34–39]. Many of the SAR inundation studies of both tidal and inland wetlands have obtained high accuracies comparing classified inundation to validation datasets, including in situ water level observations. However, these validations have largely been empirical, without assessment of microwave scattering physics which is influenced by inundation dynamics. Two techniques that characterize microwave scattering physics include (1) polarimetric decompositions that utilize measured radar backscatter intensity and phase information at different polarizations to classify scattering mechanisms [23,24], and (2) radiometric models that estimate radar scattering from different wetland structures based on vegetation structure and character of the underlying surface [40,41]. The use of either polarimetric decompositions or radiometric modeling have been limited in

assessing tidal marsh inundation state, and no studies have utilized both approaches in tandem [41–43].

In this study, we combined in situ water level observations, polarimetric decompositions, and radiometric modeling to assess the accuracy of tidal marsh inundation products developed using conventional classification approaches like backscatter thresholding and backscatter change detection. We performed this assessment across a range of sites in the Mid-Atlantic and Gulf of Mexico (Gulf Coast) United States. We used several sources of SAR imagery including Sentinel-1 C-band imagery, Phased Array type L-band Synthetic Aperture Radar (PALSAR) imagery, PALSAR-2 L-band imagery, and L-band imagery from the NASA/JPL Uninhabited Aerial Vehicle Synthetic Aperture Radar (UAVSAR) AM/PM Campaign. We compared L-band and C-band SAR inundation products to Landsat-based optical inundation products developed by the EU Joint Research Commission (JRC) [14] and the Dynamic Surface Water Extent (DSWE) product developed by the U.S. Geological Survey [15]. Our study is relevant to the NASA-ISRO SAR (NISAR) satellite mission ecosystem focus area which targets characterization of inland and coastal wetland inundation with a mission science requirement of inundation classification with a minimum of 80% accuracy at 1 hectare spatial scale and 12-day repeat (or better) [44]. Our objective is to assess a classification scheme that can be applied to NISAR L-band datasets, which will be provided for all land areas globally, to ensure that this mission science requirement is met for coastal marshes. To this end, we carried out a novel three-way analysis incorporating water level observations, SAR image analyses, and radiometric modeling to better elucidate scattering mechanisms in tidal marshes, and thus inundation product development for NISAR and other radar missions.

2. Materials and Methods

2.1. Study Sites and Water Level Sensor Deployment

Prior to the development of SAR inundation products, we established several study sites across the U.S. Mid-Atlantic and Gulf Coast regions where we had previously characterized wetland vegetation community composition and hydrologic characteristics for certain sites [45,46]. The vegetation communities are primarily emergent/herbaceous and include grasses, sedges, and rushes. A further description of vegetation characteristics is provided in Section 2.2. The sites we selected include Wheeler Marsh (CT, USA) [46], GCReW/Kirkpatrick Marsh (MD, USA) [47], Blackwater NWR (MD, USA) [48], Wax Lake Delta (LA, USA), White Lake/Chenier Plain (LA, USA), and Sabine River (LA/TX, USA) (Figure 1). We also include analyses over Great Meadows marshes (CT, USA) and Nissequogue River marshes (NY, USA) which are not shown in Figure 1, but are located in the central Long Island Sound in close proximity to Wheeler Marsh.

To validate remote sensing inundation products, we deployed grids of Onset HOBO U20L water level sensors in Wheeler Marsh and GCReW/Kirkpatrick Marsh (Figure 1, panels 1–2). Water level sensors were deployed in these systems for several months to allow for a time and water level-based calibration with nearby National Oceanic and Atmospheric Administration (NOAA) tide gauges (Bridgeport, CT, USA, NOAA station 8467150 and Annapolis, MD, USA, NOAA station 8575512, respectively). A lagged correlation analysis comparing in-marsh water level observations to NOAA tide gauge observations was then conducted to establish a time offset based on the lagged maximum R^2 value. After determining the best fit time offset, we performed a regression analysis to determine slopes and intercepts for in-marsh water levels and NOAA tide gauge water levels. Calibrations between the in-marsh water level sensors and NOAA tide gauges were highly accurate across marsh-deployed sensors (R^2 >= 0.949) (Supplementary Materials Table S1). This enabled us to accurately estimate in-marsh water level from the longer-term NOAA tidal

series, which extended the record of in-marsh water level estimates to that of our satellite record (2006–2020).

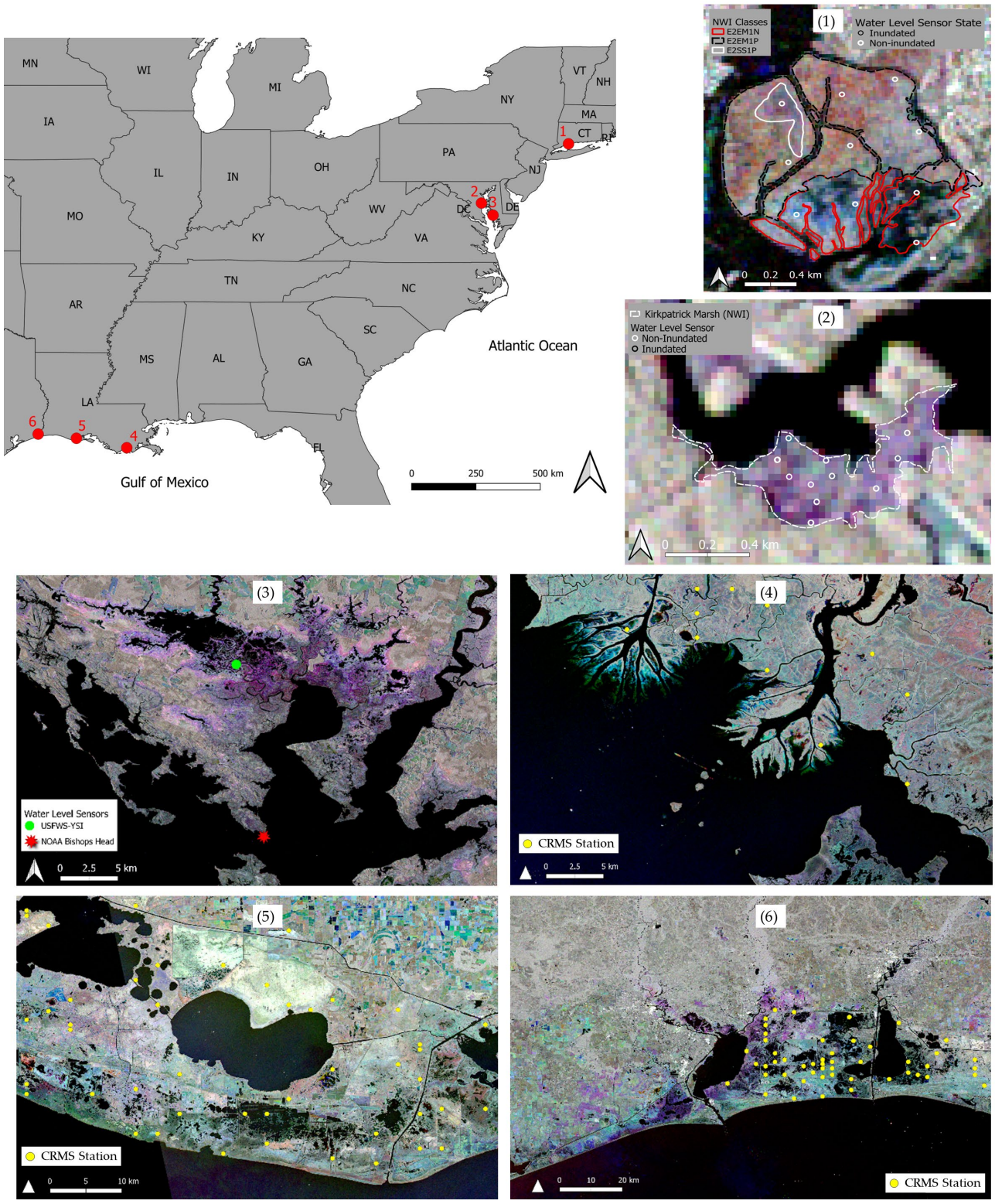

Figure 1. Study sites with Sentinel-1a VV backscatter multi-season composites (red = spring, green = summer, blue = fall) imagery and water level sensor locations (numbers in panels correspond to locations on U.S. map). Wheeler Marsh (1) and GCReW/Kirkpatrick Marsh (2) show our water level grid deployments as white symbols. Water level sensors in Blackwater NWR (3), the Wax Lake Delta (4), White Lake (5), and Sabine River (6) were deployed by other research groups.

Blackwater NWR water level observations were obtained from a U.S. Fish and Wildlife Service (USFWS) monitoring effort that ran for two months in 2016 using a Yellow Springs Instrument (YSI) measuring water levels. The YSI water level time series was compared to the Bishop's Head NOAA station (ID 8571421). The maximum R^2 value of 0.636 was obtained at a time offset of 186 min. Although this correlation is lower than Wheeler Marsh and GCReW, the difference is expected given the hydrologic complexity of the Blackwater NWR system. This time offset agrees with a previous NOAA and U.S. Army Corps of Engineers study for this site demonstrating a 120–180 min lag between the Shorter's Wharf region (where the YSI was deployed) and a less distant NOAA tidal station at McCready's Creek (ID 8571559) [48].

Study sites along the U.S. Gulf Coast were selected based on having a high density of tidal marshes as identified by previous classification efforts [46], a sufficient number of UAVSAR scenes, and water level sensor sites within the wetland systems. All selected Gulf Coast study sites were deemed to have sufficient water level sensor observations from either the State of Louisiana Coastwide Reference Monitoring System (CRMS) network or NOAA tide gauges.

2.2. Radiometric Modeling and Parameterization

To better elucidate scattering mechanisms captured in SAR image analyses (Sections 2.3–2.5), we performed several radiometric modeling simulations. We employed the Michigan Microwave Canopy Scattering (MIMICS) model which provides the ability to model microwave scattering for various vegetated landscapes including wetlands [49,50]. MIMICS allows for flexible parameterization of vegetation canopies and the underlying surfaces. Our objective was to simulate radar scattering for tidal marshes with varying surface hydrologic states for C-band and L-band wavelengths.

Tidal marsh vegetation is herbaceous and primarily comprised of stems and leaves in terms of above-ground biomass. Because leaves and stems are primarily vertically structured, we parameterized these components with an erectophile-type geometry distributions in MIMICS. We reviewed marsh vegetation allometric studies, finding they generally focused on *Typha* spp. (Cattails, common to freshwater tidal and oligohaline marshes), *Spartina alterniflora* (Smooth Cordgrass, common to low elevation brackish and salt marshes), and *Phragmites australis* (Common Reed, a U.S. invasive found across marshes of mid-high elevation) [51–56]. To establish generalized vegetation parameters representative of a tidal marsh, we combined findings from these published studies with our own wetlands allometric measurements. We parameterized marsh vegetation stems with a 1.5 cm diameter (based on our field measurements of *Typha* spp., n = 5). Leaves were parameterized with a 2.5 cm diameter and primarily vertically oriented. The generalized marsh canopy was modeled with 200 leaves/m^3 and 50 stems/m^3. Our study used stem density of 50 stems/m^3 to represent an intermediate value between the literature-identified areal stem density of *Typha* spp. (~25 stems/m^2 [51]), *Phragmites australis* (~70–80 stems/m^2 for moderate density stands [52]), and tall-form *Spartina alterniflora* (113 stems/m^2 [53]), while also considering that the larger stem diameters of *Typha* spp. and *Phragmites australis* correspond to lower stem densities than *Spartina alterniflora*. We parameterized MIMICS with a stem density (stems/m^3) rather than the areal densities reported in the literature as this allowed us to vary canopy heights while keeping stem densities fixed.

Tidal marsh canopy heights were parameterized in MIMICS based on our field measurements, which found that higher biomass marsh vegetation like *Phragmites australis* and *Typha* spp. had average canopy heights of 1.977 m (n = 25). Tall-form *Spartina alterniflora* has also been found to reach heights of 2.137 m [57]. Our field sampling indicated more variation in lower biomass species (*Spartina patens*, short-form *Spartina alterniflora*, and

Schoenoplectus americanus) ranging from 0.229 m to 1.803 m, albeit with fewer samples (n = 6). Due to limitations in field sampling for lower biomass species, we parameterized MIMICS with approximated canopy heights varying between 0.5, 1.0, and 2.0 m.

Compared to the generalized vegetation dimensions, more precise vegetation water content values were used in MIMICS. Our field sampling for growing season and non-growing season vegetation water contents were quite consistent with average values of 66.56% (SD = 9.08%, n = 72) and 17.50% (SD = 9.87%, n = 57), respectively. These values were used to represent seasonal vegetation water content cases.

In total, there were six vegetation parameterizations of the MIMICS model with three vegetation height cases (0.5, 1.0, and 2.0 m) and two seasonal vegetation water content cases. We parameterized MIMICS with a rough ground surface in all cases, which we observed across our tidal marsh study sites. The surface was parameterized with root-mean-square height of 2 cm and a gaussian autocorrelation length parameter of 10 cm, identical to those used to represent a tidal marsh in a radiometric modeling study by Duan and Jones (2017) [58]. In our effort, we represented marsh soil as equal proportions of sand, silt, and clay.

The primary motivation of the MIMICS effort was to determine how sub-canopy hydrologic variability influences SAR backscatter intensity. To assess effects of changing hydrologic state in MIMICS, we varied marsh soil moisture from 0% to 100% in 5% increments. After a soil moisture of 100%, the MIMICS soil model was replaced with a water surface layer model with a salinity of 20 parts per thousand. We then iteratively increased the water layer height, progressively submerging the marsh canopy to the point of complete submergence. For each of six vegetation cases and their corresponding iterative hydrologic simulations, we simulated C-band scattering from the Sentinel-1 satellite and L-band scattering from the PALSAR/PALSAR-2 satellites.

MIMICS models total backscatter power and contributions to backscatter from various types of scattering mechanisms which include direct ground scattering, direct crown (i.e., canopy) scattering, crown–ground (and ground–crown), as well as crown–ground–crown scattering (Figure 2). In order to assess the most challenging case for radar detection of surface hydrologic state, we focused our analysis on the simulations with 2.0 m canopy height and growing season vegetation water content (66.57%). In doing so, we evaluated C-band and L-band response for a moderate-high biomass marsh where vegetation water content and structure are most likely to interfere with radar signal surface interaction, and thus characterization of inundation state.

2.3. Image Assembly and Processing

We assembled a 2006–2020 multi-sensor SAR dataset to evaluate capabilities in characterizing marsh inundation state. PALSAR/PALSAR-2, UAVSAR, and Sentinel-1a imagery were all used in this assessment. Additionally, JRC and DSWE optical inundation products were compared to the SAR-based inundation products and assessed against in situ water level observations. Optical spectral indices (NDWI [11] and mNDWI [12]) were also compared to SAR backscatter in terms of correlation with water level observations for different marsh types.

Sentinel-1 backscatter imagery was acquired from Google Earth Engine (GEE) where it had been processed with ESA's SNAP toolbox for calibration and radiometric terrain correction prior to GEE ingestion. The SNAP toolbox was also used for the processing of PALSAR-2 backscatter imagery, performing calibration, multi-looking, speckle filtering, and radiometric terrain corrections. Multi-looking PALSAR-2 imagery was performed with the least number of looks required to produce a quasi-square pixel. Generally, this meant use of a 4 × 2 or 5 × 2 window depending on whether images were acquired in High-

sensitive Beam Quad (HBQ) or Fine Beam Dual (FBD) mode, respectively. Multi-looking in this manner served to reduce speckle noise while still preserving a pixel resolution of 8.5 m or finer. Additional speckle filtering was then performed using a 5 × 5 Enhanced Lee filter. Radiometric terrain correction was performed with a 30 m version of the Shuttle Radar Topography Mission Digital Elevation Model (DEM). PALSAR backscatter imagery (FBD mode) was acquired from the Alaska Satellite Facility (ASF) at the 1.5 processing level with a pixel resolution of 12.5 m or finer, where it had been previously calibrated and radiometric terrain corrected. After downloading PALSAR imagery from ASF, it was speckle-filtered with a 5 × 5 Enhanced Lee filter.

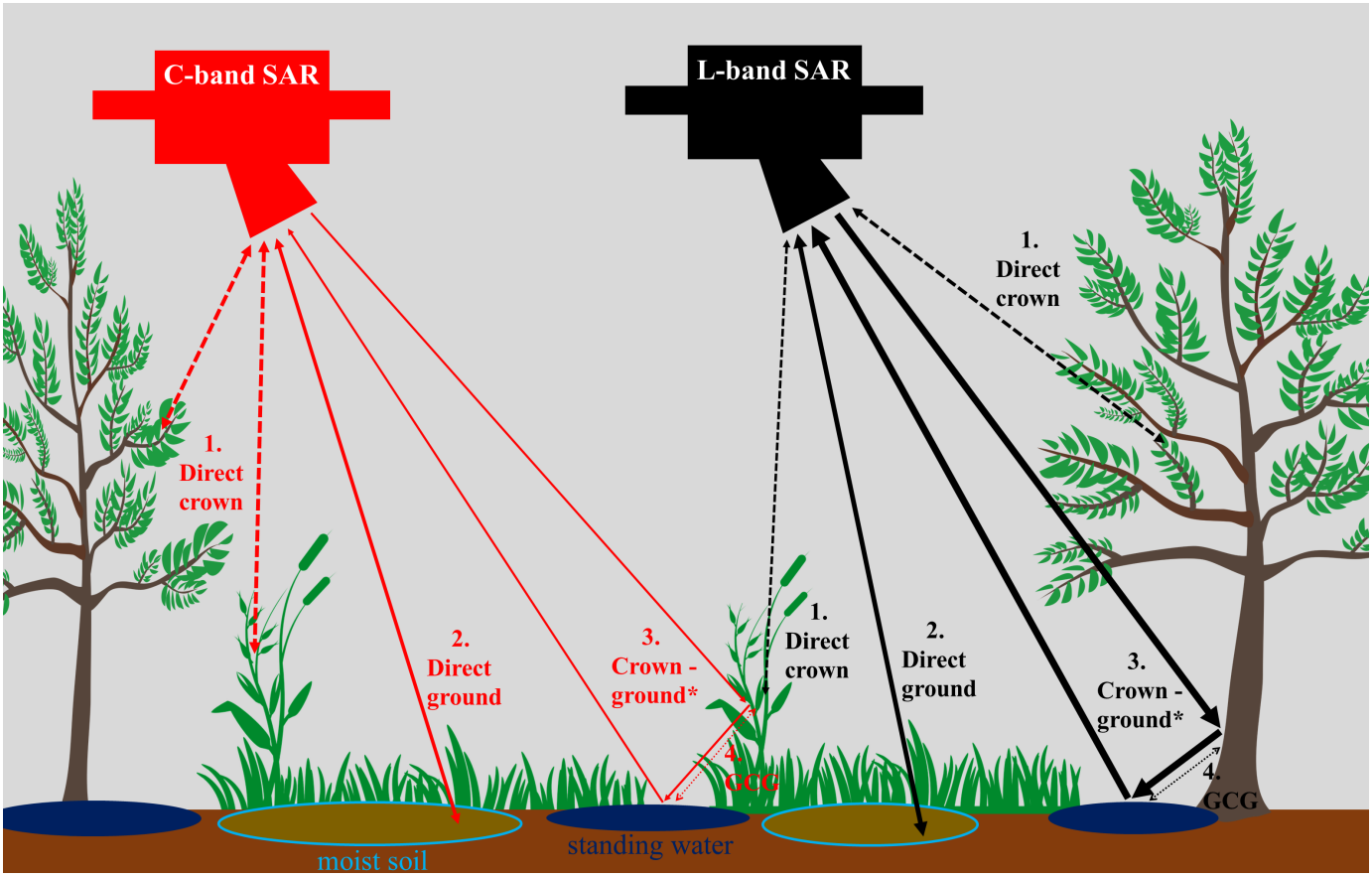

Figure 2. Depictions of generalized scattering mechanisms for C-band and L-band SAR when imaging wetlands. The primary types of radar scattering interactions that are modeled in MIMICS for a wetland system, ordered by increasing scattering coherence include direct crown (i.e., direct canopy) scattering (1), direct ground scattering (2), and crown–ground scattering (3). Double-bounce scattering includes both crown–ground and ground–crown scattering directions (* schematic depicts only crown–ground). A secondary scattering component modeled in MIMICS is the crown–ground–crown interaction (4) which is depicted by the dotted two-direction arrow near the crown–ground depiction. A generalization of SAR signal backscatter intensity is depicted by line thickness. Dashed lines depict volume scattering as opposed to surface or double-bounce scattering.

UAVSAR quad-polarimetric imagery was acquired from ASF in Ground Projected Complex format and processed with PolSARpro software (v6.0) and ASF's MapReady software using a routine of computing T3 coherency matrices, performing polarimetric speckle filtering with a 5 × 5 window, and performing polarimetric decompositions. For quad-polarimetric PALSAR-2 imagery, the same processing sequence was utilized.

Sentinel-1 imagery was regularly acquired at 12-day intervals at approximately 6 pm local time over the Mid-Atlantic study sites between 2016 and 2020, which provided us

with a dense time series for analysis. PALSAR/PALSAR-2 and UAVSAR images were acquired less frequently than Sentinel-1 but were used more commonly in the proceeding analysis. For these reasons, PALSAR/PALSAR-2 and UAVSAR images are listed in Table 1, but Sentinel-1 image descriptions been omitted for the sake of brevity and are instead included in Supplementary Materials Table S2.

Table 1. L-band PALSAR/PALSAR-2 and UAVSAR acquisitions. Tidal stage column is the closest NOAA gauge water level observation for an image covering a study site. Wheeler and Blackwater NWR tidal stages have been time-adjusted (Supplementary Materials Table S1). Underlined cells with parentheses represent the previous maximum tidal stage two days or less prior to image acquisition. Sentinel-1a images were acquired at a highly consistent 12-day repeat between 2016 and 2020, and are listed in Supplementary Materials Table S2 along with additional information on PALSAR images.

Sensor	Acquisition Time (GMT)	Site	Polarization	Tidal Stage (Meters)
PALSAR	26 September 2007 03:16:00	Wheeler	HH, HV	2.313
PALSAR	16 August 2009 03:18:00	Wheeler	HH, HV	0.884
PALSAR	19 November 2010 03:15:00	Wheeler	HH, HV	1.737
PALSAR-2	25 April 2016 17:02:00	Wheeler	HH, HV	1.951
PALSAR-2	24 April 2017 17:03:00	Wheeler	HH, HV	1.305
PALSAR-2	27 April 2017 4:40:00	Wheeler	HH, HV, VH, VV	2.582
PALSAR-2	6 November 2017 17:02:00	Wheeler	HH, HV	2.807
PALSAR	5 December 2006 03:30:00	Blackwater	HH	0.128 (0.561)
PALSAR	15 March 2010 03:32:00	Blackwater	HH	0.579 (1.164)
PALSAR-2	10 May 2015 4:56:00	Blackwater	HH, HV, VH, VV	0.302
PALSAR-2	7 May 2017 4:52:00	Blackwater	HH, HV, VH, VV	0.777
UAVSAR	13 August 2019 21:56:25	Wax Lake	HH, HV, VH, VV	0.622 (0.841)
UAVSAR	1 October 2019 21:59:22	Wax Lake	HH, HV, VH, VV	1.006 (1.091)
UAVSAR	1 July 2019 14:02:30	White Lake	HH, HV, VH, VV	0.780 (0.924)
UAVSAR	16 July 2019 12:47:28	White Lake	HH, HV, VH, VV	0.808 (1.716)
UAVSAR	12 August 2019 13:42:28	Sabine River	HH, HV, VH, VV	0.497
UAVSAR	23 September 2019 13:21:08	Sabine River	HH, HV, VH, VV	0.939

2.4. Backscatter Inundation Product Development

The SAR inundation products we developed in a previous study utilized backscatter change detection and threshold classification approaches [45]. However, these approaches were applied only to a single site in each case. A change detection classification approach developed for time-series C-band Sentinel-1a imagery over GCReW showed that a backscatter temporal standard deviation (SD) > 1.5 effectively classified marsh inundation. In that previous study, we employed a backscatter threshold classification for L-band PALSAR imagery for Blackwater NWR, classifying marsh inundation where HH backscatter < −13.5 dB. In both of these cases, validation was limited to in situ water level observations.

In this study, we expanded on previous efforts in several ways. First, we assessed backscatter correlations with water level across five study sites (Blackwater NWR, GCReW, Wheeler Marsh, Great Meadows, and Nissequogue River). We used USFWS National Wetlands Inventory (NWI) polygons to compute spatial averages of backscatter and optical indices for this correlation analysis. We employed a similar Sentinel-1 C-band image change detection classification over Wheeler Marsh as our previous efforts but refined the approach by including both VH and VV/VH channels. Wheeler Marsh served as a target study site for a full comparison of L-band, C-band, and optical inundation product performance due to availability of imagery. For Wheeler Marsh, we derived conceptual inundation depth products from L-band imagery and a high-resolution DEM, using a bathtub model. Third, we developed an improved thresholding approach by evaluating PALSAR/PALSAR-2 L-band backscatter time series over Wheeler Marsh and incorporating both HH and HV

channels (justification is shown in Figure 3). The final threshold-based classification for L-band SAR imagery is shown in Equation (1), where inundation is classified using the backscatter from HH polarization imagery (σ^0_{HH}) and HV polarization imagery (σ^0_{HV}).

$$\text{Inundated pixel} = \left(\sigma^0_{HH} < -14.0\ \text{dB}\right) \,\&\, \left(\sigma^0_{HV} < -23.0\ \text{dB}\right) \quad (1)$$

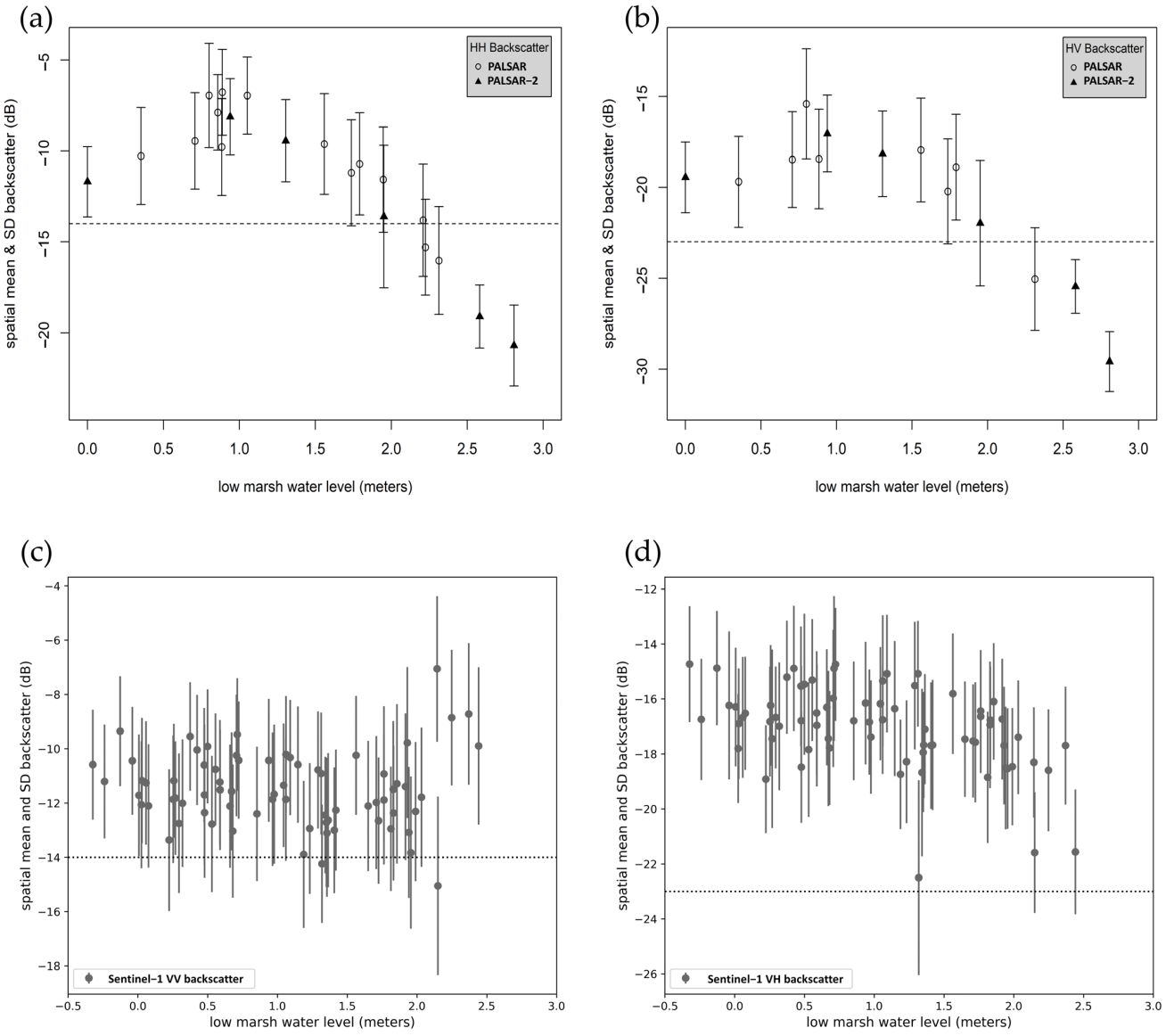

Figure 3. PALSAR/PALSAR-2 L-band HH (**a**) and HV (**b**) polarizations compared to Sentinel-1 C-band VV (**c**) and VH (**d**) polarizations (2016–2019) as a function of Wheeler Marsh tidal stage for low-mid elevation marsh region dominated by dense *Spartina alterniflora* (NWI class E2EM1P). Horizontal lines are positioned at the pixel inundation thresholds of −14.0 dB for co-polarizations and −23.0 dB for cross-polarizations. PALSAR imagery shows complete separability for the lowest and highest tide imagery in both co- and cross-polarizations. Backscatter distributions are +/−1 standard deviation (SD) for each point.

In contrast to Wheeler Marsh, for many of the study sites a comparison of time-series L-band and C-band imagery was not possible as L-band imagery availability was often more limited. In these cases, we selected low tide and high tide image pairs for comparison. This was the case for Blackwater NWR, Wax Lake Delta, White Lake, and the Sabine River. For Blackwater NWR, we performed an additional low tide–high tide backscatter distribution comparison to assess consistency with the Wheeler Marsh analysis. Backscatter

threshold classifications were applied to these low tide–high tide image pairs, with many of the images being quad-polarimetric and classified with polarimetric decompositions characterizing scattering mechanisms, as described in the following section.

2.5. Polarimetric Decompositions Derived from Quad-Polarimetric SAR

We acquired complex quad-polarimetric (HH, HV, VH, VV) PALSAR-2 imagery for Wheeler Marsh and Blackwater NWR, including a low tide–high tide image pair for Blackwater NWR. Several quad-polarimetric (HH, HV, VH, VV) UAVSAR AM/PM Campaign scenes were acquired over the Wax Lake Delta, White Lake, and Sabine River study sites. For the UAVSAR analysis, we selected low tide–high tide image pairs for each site with the closest possible acquisition times to reduce the impacts of vegetation seasonality. Polarimetric decompositions, incorporating phase and intensity information, were applied to the quad-polarimetric images as this approach offers some of the best performance in assessing emergent wetland inundation state for single-date images [59]. We used the van Zyl decomposition which decomposes odd-bounce scattering (dominated by surface scattering), even-bounce scattering (dominated by double-bounce), and volume scattering (primarily attributable to multiple scattering by vegetation) [60,61]. Polarimetric decompositions were only performed on complex quad-polarimetric SAR imagery since dual-polarimetric decompositions are far less effective at accurately identifying these three scattering mechanisms [62]. Secondly, we applied threshold-based classifications (Equation (1)) to the same quad-polarimetric images to assess performance comparison between backscatter-based and polarimetric decomposition-based tidal marsh inundation classifications. The quad-polarimetric decompositions and threshold-based classifications were compared for different tidal stages when multiple images were available.

3. Results

3.1. Overview of Results

Results from our evaluation of L-band SAR, C-band SAR, and optical index responses to changes in tidal marsh inundation state are discussed in detail in Section 3.2. These findings inform the selection of optimal backscatter thresholds for classification of SAR imagery (Equation (1), Figure 3). In Section 3.3, we present classified inundation extent maps for Wheeler Marsh with water level sensor grids providing validation. We compare C-band and optical results from Wheeler Marsh to results from GCReW from our previous studies. In Section 3.4, we compare the empirical findings from Sections 3.2 and 3.3 to the results of the MIMICS radiometric modeling effort to identify changes in scattering mechanisms in response to changes in tidal marsh inundation state. In Section 3.5, we further evaluate SAR scattering mechanisms by performing polarimetric decompositions on quad-polarimetric L-band PALSAR-2 and UAVSAR imagery and comparing decompositions to backscatter threshold inundation classifications.

3.2. Backscatter and Tidal Stage Relationships

We found that L-band backscatter was a stronger correlate to tidal stage than C-band backscatter or optical indices across several marsh sites (Table 2). The Wheeler Marsh NWI E2EM1N class, which corresponds to a mix of mudflat and sparse *Spartina alterniflora*, exhibited similar degrees of tidal stage correlation between optical water indices (NDWI and mNDWI) and L-band SAR backscatter. However, for the Wheeler Marsh E2EM1P NWI class with dense *Spartina alterniflora* and *Scirpus* spp., the optical water index correlation dropped significantly whereas L-band backscatter did not. C-band correlation with tidal stage varied between sites but was generally highest for the VV/VH polarimetric ratio over Blackwater NWR, and the VH channel for all other sites.

Table 2. Sentinel-1 (S1) and PALSAR/PALSAR-2 (PLSR) correlation with tidal stage (expressed as *R* values) (all available satellite imagery through 2019). OLS represents linear least squares fit between NWI polygon-averaged backscatter and tidal stage. Poly represents a second order polynomial fit. Absolute *R* values greater than 0.8 have been bolded. Only two PALSAR low tide–high tide image pairs were available for Blackwater NWR, and no high tide images were available for GCReW; therefore, no correlation assessment was performed.

Study Site	NWI Class	S1-VH OLS	S1-VH Poly	S1-VV OLS	S1-VV Poly	S1-VV/VH OLS	S1-VV/VH Poly	NDWI OLS	NDWI Poly	mNDWI OLS	mNDWI Poly	PLSR-HH OLS	PLSR-HH Poly	PLSR-HV OLS	PLSR-HV Poly
Blackwater	E2EM1N	−0.64	0.76	0.37	0.58	−0.71	**0.89**	0.31	0.38	0.46	0.47	--	--	--	--
Blackwater	E2EM1P	−0.69	0.76	0.58	0.67	−0.77	**0.86**	0.35	0.39	0.47	0.52	--	--	--	--
Blackwater	E2EM1P6	−0.45	0.54	0.37	0.38	−0.53	0.57	0.19	0.28	0.00	0.24	--	--	--	--
Blackwater	E2EM1Pd	−0.65	0.73	0.46	0.54	−0.68	0.77	0.41	0.41	0.56	0.67	--	--	--	--
Blackwater	E2SS4P	−0.19	0.42	0.40	0.40	−0.46	0.46	0.05	0.30	−0.07	0.08	--	--	--	--
Blackwater	E2FO4P	−0.09	0.36	0.36	0.38	−0.40	0.40	0.01	0.24	0.11	0.14	--	--	--	--
GCReW	E2EM1P	−0.28	0.32	0.57	0.78	−0.67	**0.88**	−0.48	0.48	0.28	0.30	--	--	--	--
Wheeler	E2EM1N	**−0.83**	**0.88**	−0.78	0.79	0.45	0.47	**0.91**	**0.92**	**0.91**	**0.91**	**−0.85**	**0.88**	**−0.92**	**0.98**
Wheeler	E2EM1P	−0.40	0.43	0.01	0.27	−0.29	0.50	0.56	0.64	0.70	0.77	**−0.81**	**0.96**	−0.63	**0.92**
G. Meadows	E2EM1N	−0.67	0.73	−0.43	0.43	−0.25	0.41	**0.85**	**0.89**	--	--	**−0.82**	**0.94**	−0.72	**0.90**
G. Meadows	E2EM1P	−0.47	0.56	−0.08	0.11	−0.38	0.50	0.69	0.78	--	--	−0.72	**0.87**	−0.67	**0.82**
Nissequogue	E2EM1N	**−0.83**	**0.88**	−0.76	0.76	0.42	0.45	--	--	--	--	−0.67	0.74	**−0.84**	**0.95**
Nissequogue	E2EM1P	−0.40	0.43	−0.08	0.30	−0.41	0.59	--	--	--	--	−0.54	0.68	−0.45	**0.85**
Nissequogue	E2EM5P	−0.18	0.19	−0.23	0.24	0.06	0.09	--	--	--	--	−0.47	0.70	−0.63	**0.87**

The findings from Table 2 and Figure 3, along with previous results [45], supported the implementation of threshold-based classifications for L-band imagery but not C-band imagery. Figure 3 depicts clear decreases in L-band backscatter distributions as a function of tidal stage, which become separable when comparing regular low tides to regular high tides. C-band distributions lacked separability, though the VH channel showed a fairly consistent decrease in backscatter as a function of tidal stage, supporting the use of change detection approaches for classifying tidal marsh inundation. These findings for Wheeler Marsh in Long Island Sound were consistent with those of the Chesapeake Bay tidal marshes comparing C-band and L-band SAR [45].

3.3. Inundation Product Validation

The validation accuracy of inundation products over Wheeler Marsh are listed in as follows: JRC optical inundation product (40%, 4/10) (Figure 4a), DSWE optical inundation product (90%, 9/10) (Figure 4b), C-band change detection classification (88.8%, 71/80) (Figure 5), and L-band threshold classification (90%, 54/60) (Figure 6). GCReW validation performance was as follows: JRC optical inundation product (0%, 0/11), DSWE inundation optical product (27.3%, 3/11), and C-band change detection (76.4%, 84/110). High tide L-band SAR imagery over GCReW was not available for analysis. Additional GCReW validation maps and further description of analyses are provided in [63].

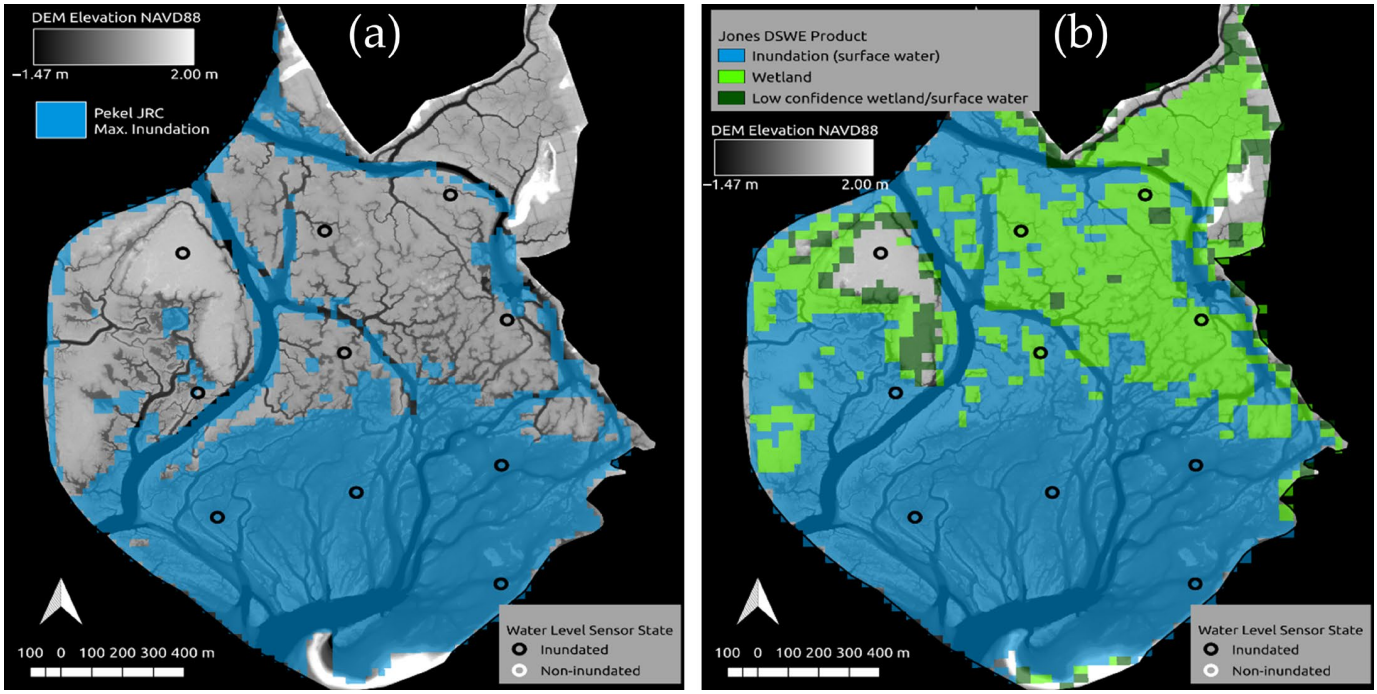

Figure 4. Optical inundation products derived from Landsat imagery over Wheeler Marsh at high tide (>=2.124 m). JRC maximum surface water extent computed over the Landsat 5–8 record (1985–2019) is shown in (**a**). Four out of ten water level sensors matched classified inundation from the JRC product. (**b**) The DWSE product derived from a single high–tide Landsat image from 1 December 2018. The DSWE product contains a more complex classification scheme than JRC in which 9/10 sensors corresponded to detected inundation as surface water or wetland classes.

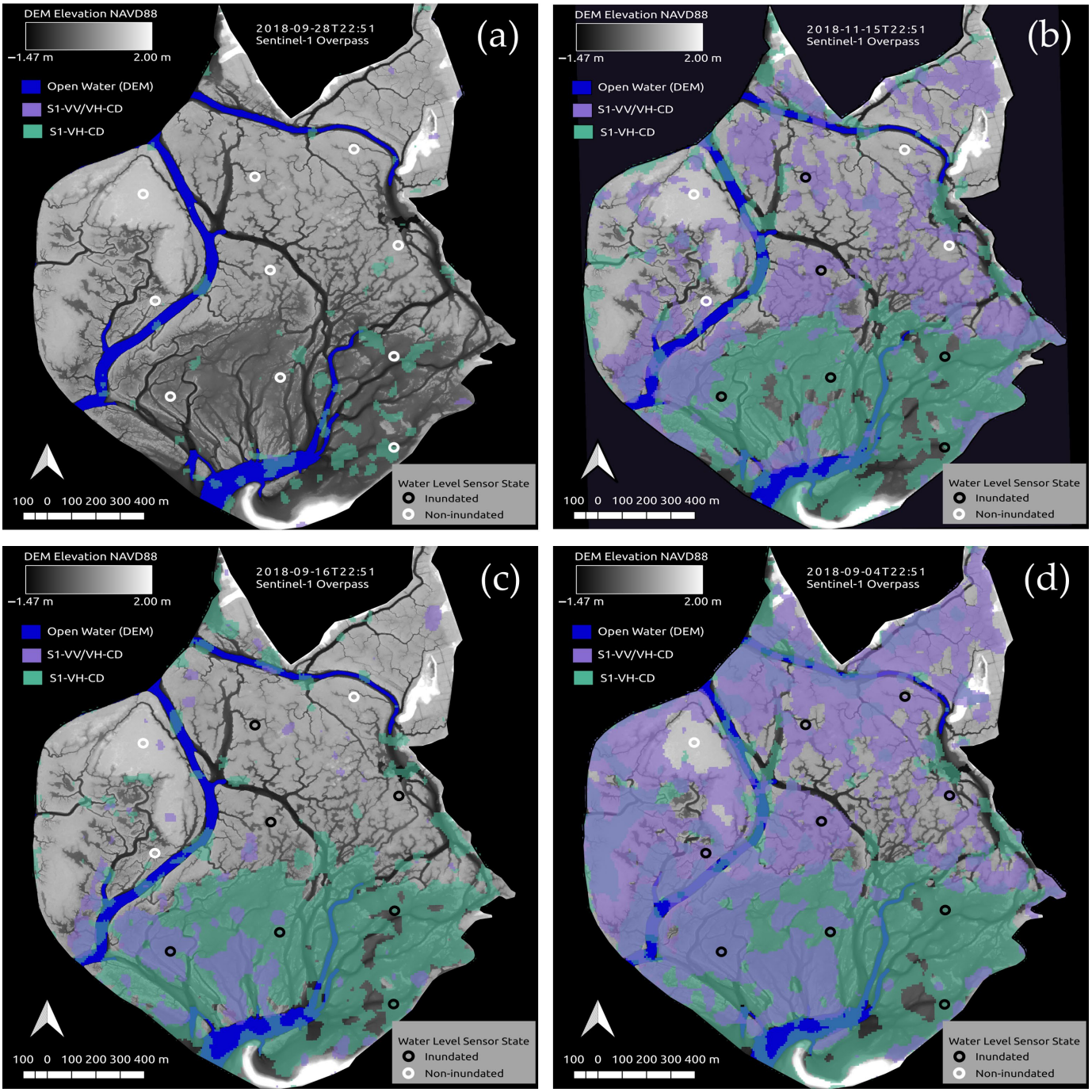

Figure 5. Sentinel-1 C-band change detection (CD) inundation products over Wheeler Marsh. Classified 88.8% classification accuracy comparing SAR inundation products to in situ water level sensor inundation state (71/80) for eight total images. Four example images shown in (**a**–**d**) correspond to increasing tidal stage.

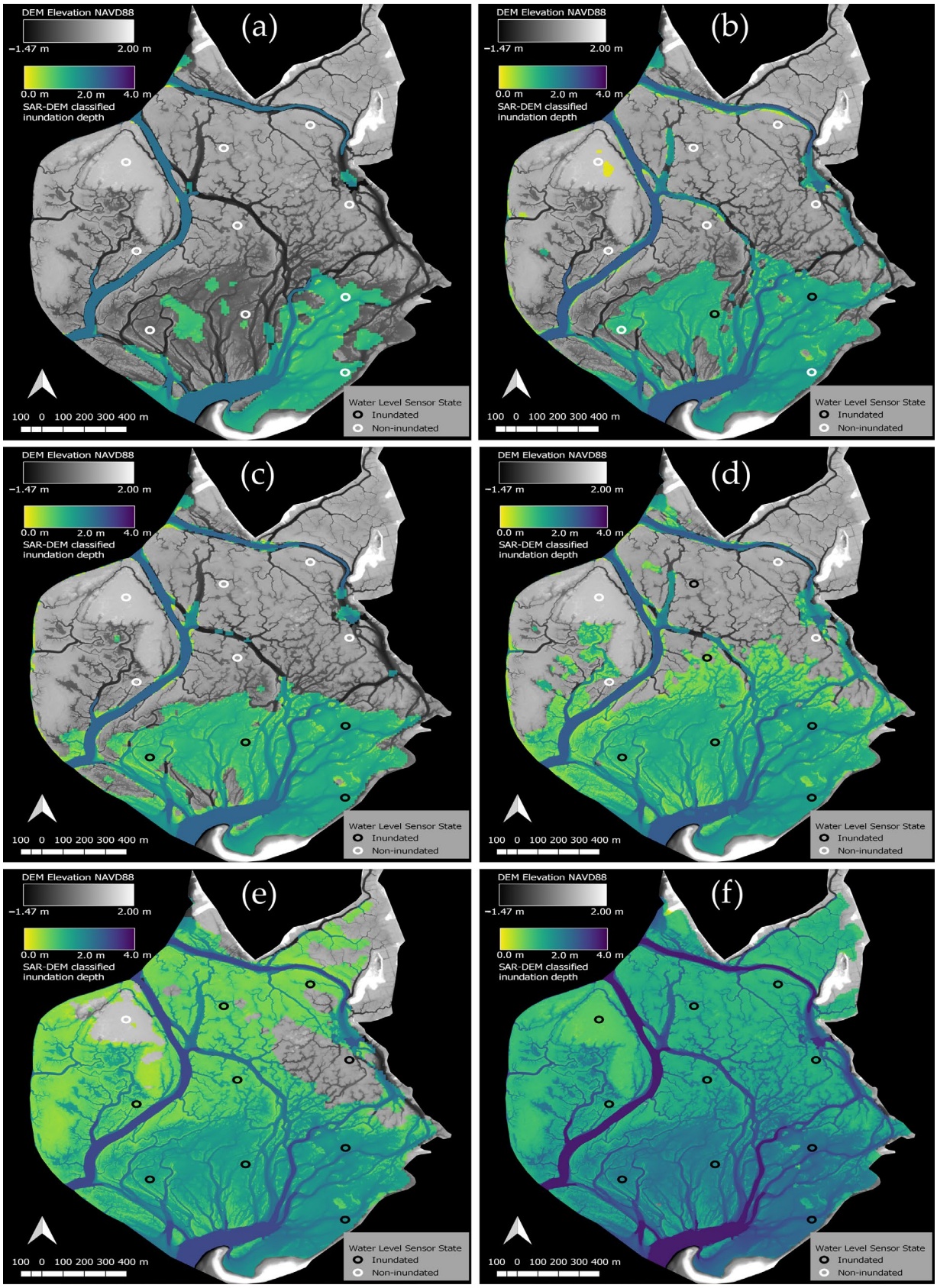

Figure 6. PALSAR-1/2 L-band threshold-based inundation products over Wheeler Marsh. Inundation is classified where HH < −14.0 dB and HV < −23.0 dB (Equation (1)). 90% classification accuracy comparing SAR inundation products to in situ water level sensor inundation state (54/60). Panels (**a**–**f**) are ordered by increasing tidal stage. The Viridis color scale represents approximate water depth of inundated pixels.

3.4. MIMICS Radiometric Modeling Results

MIMICS was used to elucidate differences between C-band and L-band radar scattering mechanisms in tidal marshes and to provide explanatory context for the findings in the preceding Sections 3.2 and 3.3. MIMICS simulations (Figures 7–9) show modeled backscatter as a function of increasing soil moisture with the surface transitioning to an inundated state.

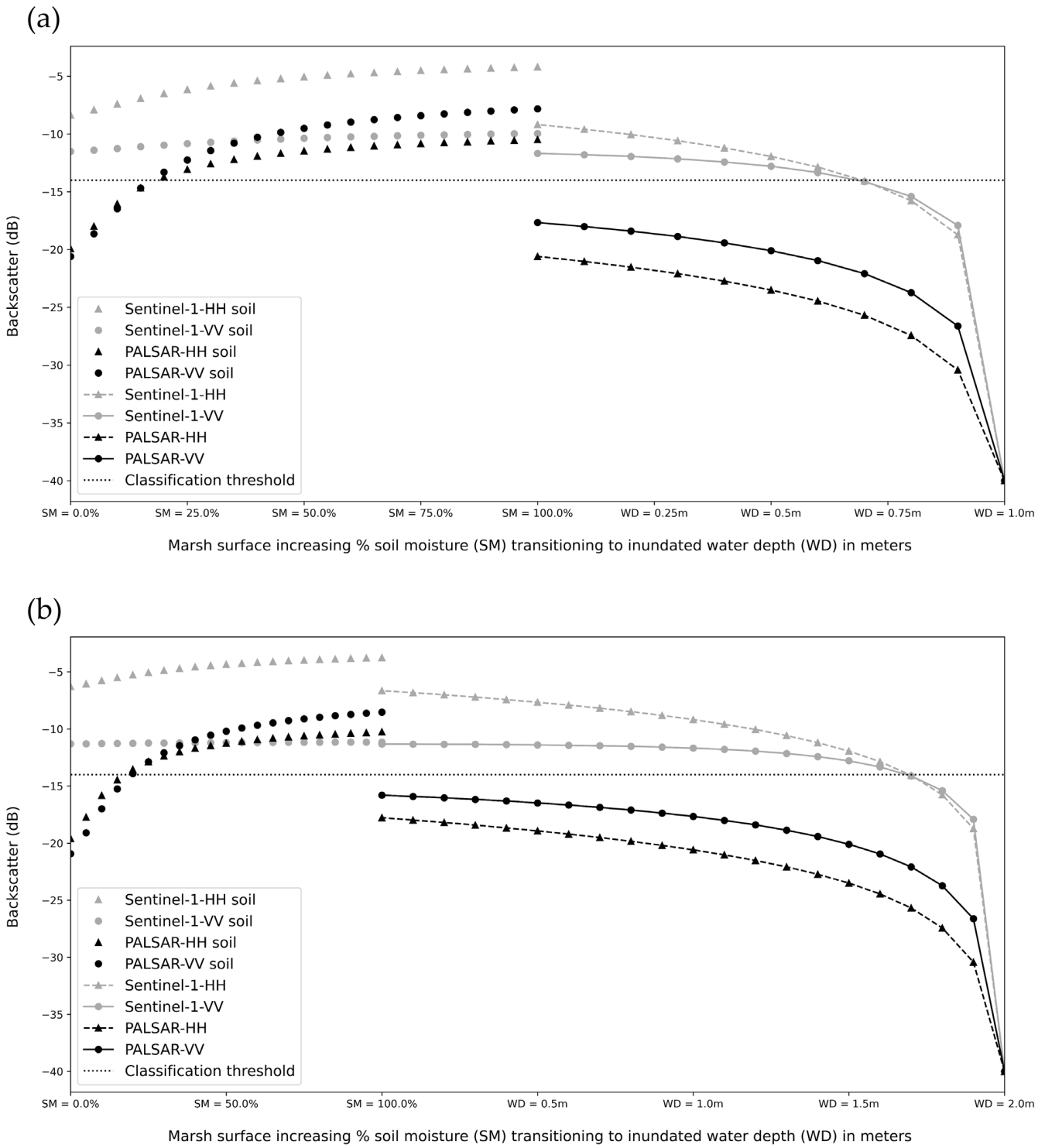

Figure 7. MIMICS simulated total backscatter response for L-band PALSAR and C-band Sentinel-1 for 1 m and 2 m vegetated marsh canopies during the growing season ((**a**,**b**), respectively). The horizontal dotted line depicts the location used in threshold-based classification in Equation (1).

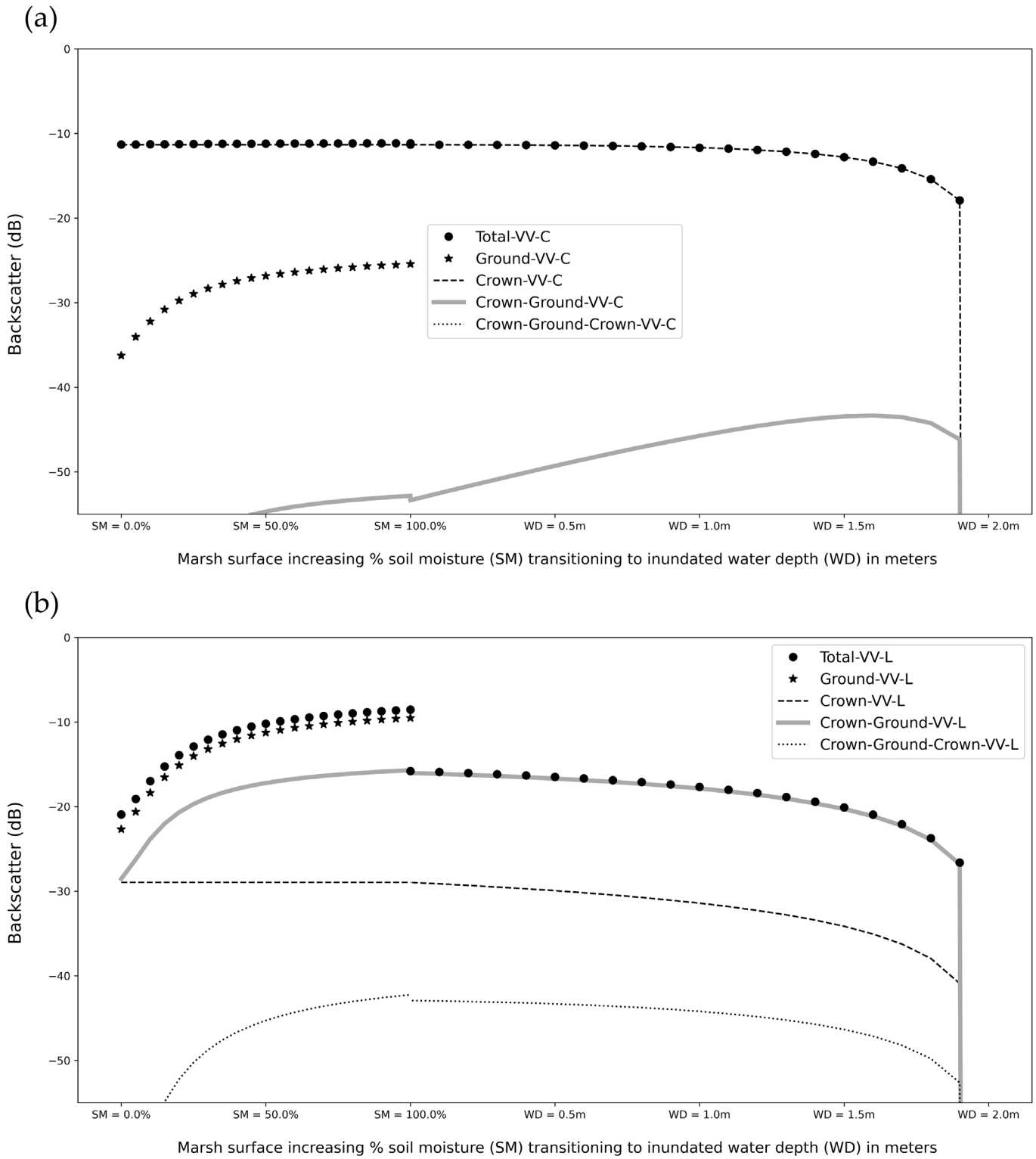

Figure 8. C-band (**a**) vs. L-band (**b**) VV backscatter contributions from different scattering mechanisms for a marsh with a 2 m canopy height. Note that decibel units sum non-linearly for total scattering.

Figure 7 demonstrates that L-band backscatter has a higher sensitivity to changes in surface hydrologic state than C-band backscatter, showing a pronounced decrease as the marsh surface transitions to inundated. For a tidal marsh with a 1 m canopy height (Figure 7a), L-band HH backscatter decreased over 10 dB while C-band VV backscatter decreased approximately 2 dB, providing an indication of sensitivity for common observation modes of PALSAR/PALSAR-2 and Sentinel-1, respectively. C-band HH backscatter

exhibited a greater decrease than C-band VV but was still less pronounced than at L-band. L-band backscatter showed similar sensitivity for a 2 m canopy height (Figure 7b), while C-band VV backscatter did not exhibit substantial change transitioning from moist soil to an inundated surface. Figures 8 and 9 illustrate contributions of different scattering sources to the total backscatter observed by a given sensor as depicted previously in Figure 2.

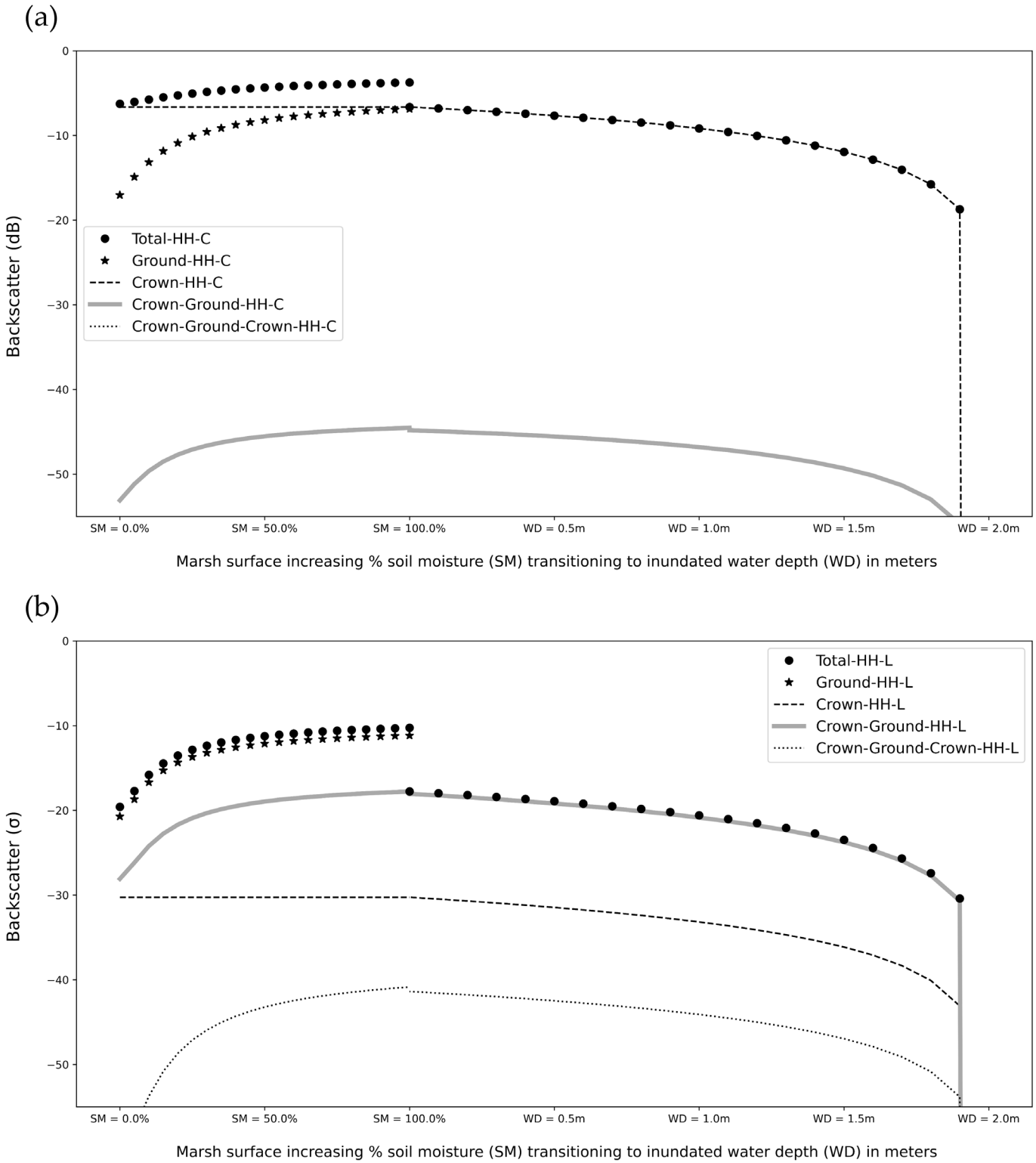

Figure 9. C-band (**a**) vs. L-band (**b**) HH backscatter contributions from different scattering mechanisms for a marsh with a 2 m canopy height. Note that decibel units sum non-linearly for total scattering.

Figure 8 shows the differences in radar scattering mechanisms that occur between L-band and C-band in the VV polarization. These differences in scattering contributions are wavelength-dependent and change according to inundation state. C-band exhibits dominant crown scattering that changes as a function of canopy submergence, while L-band backscatter exhibits dominant double-bounce scattering as a combination of ground–crown and crown–ground scattering components. For L-band VV backscatter, the scattering contributions are primarily from ground scattering before the soil transitions to an inundated surface.

Figure 9 depicts HH backscatter components similarly to the VV backscatter in Figure 8. The primary differences in scattering contributions are wavelength-dependent, with L-band exhibiting double-bounce (crown–ground and ground–crown) scattering with marsh inundation. C-band exhibits dominant crown scattering when inundated, changing as a function of canopy submergence. Compared to VV scattering (Figure 8), a key difference in Figure 9 is that C-band HH exhibits far greater ground scattering contributions than C-band VV indicating greater canopy penetration for the HH polarization.

The results of our radiometric modeling are consistent with empirical findings in [35], the authors of which found that L-band backscatter imagery characterized marsh inundation state more accurately than C-band backscatter imagery. Our simulations demonstrate that total L-band backscatter for both VV and HH channels is dominated by direct ground scattering until the marsh inundates, at which point total backscatter decreases and the remaining backscatter contributions are dominated by ground–crown and crown–ground (i.e., double-bounce) scattering, which is largely a coherent form of scattering. In contrast, direct scattering from canopies or a rough ground surface, as observed with C-band simulations, tends to produce incoherent phase returns, which has important implications for wetland Interferometric SAR (InSAR) studies.

3.5. Polarimetric Decompositions and Threshold-Based Classification Comparisons

This section presents comparisons between threshold-based inundation classification approaches and polarimetric decompositions applied to low tide–high tide image pairs linking the empirically based inundation classifications (Section 3.3) and the radiometric modeling efforts (Section 3.4). According to the findings of the MIMICS radiometric modeling, L-band imagery should exhibit a decrease in total backscatter (Figure 7) and a relative shift to double-bounce scattering (Figures 8 and 9) when tidal marshes become inundated prior to the point of canopy submergence.

The results for Wheeler Marsh shown in Figure 10 indicate that for tidal marsh sites with a large tidal range (~3 m), vegetation may submerge completely, resulting in SAR scattering signatures similar to open water where single-bounce, double-bounce, and volume scattering are all low. In contrast, the Blackwater NWR site with a lower tidal range (~1 m), shows different scattering during high tide in Figure 11 where double-bounce scattering is prominent. However, it is important to note that even when the degree of tidal marsh vegetation submergence and scattering mechanisms differ between sites at high tide, the threshold-based inundation products still capture changes in marsh inundated area effectively with L-band imagery. Further, the Blackwater NWR backscatter distribution assessment (Figure 12) indicates that distributions can be clearly distinguished between low tide and high tide for tidal marshes. Figure 12 demonstrates that the inundation classifications of open water may be more challenging than marshes due to wave- and wind-roughened surfaces producing high backscatter values compared to the smoother water surfaces below marsh canopies resulting from flow attenuation. This is particularly true for the HH channel compared to the HV channel.

The UAVSAR analysis for Gulf Coast sites is consistent with results from Wheeler Marsh and Blackwater NWR, illustrating a greater inundated area when comparing high tide and low tide imagery. For the Sabine River site, a very prominent shift to double-bounce scattering was found in the high tide van Zyl polarimetric decomposition, also corresponding to significant increases in classified inundated area and increases in CRMS water levels (Figure 13). The Wax Lake Delta analysis also shows greater inundated area in the southern portion of the high tide image (Supplementary Materials Figure S1), though there are some limitations in interpretation as vegetation phenology and seasonal hydrological changes are pronounced for this site. Over the White Lake region, increases in inundated area are present in the southeast portion of the high tide image (Supplementary Materials Figure S2). There is also an apparent shift to double-bounce scattering in this region of high tide polarimetric decomposition. The White Lake site results also demonstrate an importation limitation of the backscatter threshold classification where the near range portions of the UAVSAR swath (25–30 degrees off nadir) are not properly classified as inundated over open water (S3 & S4).

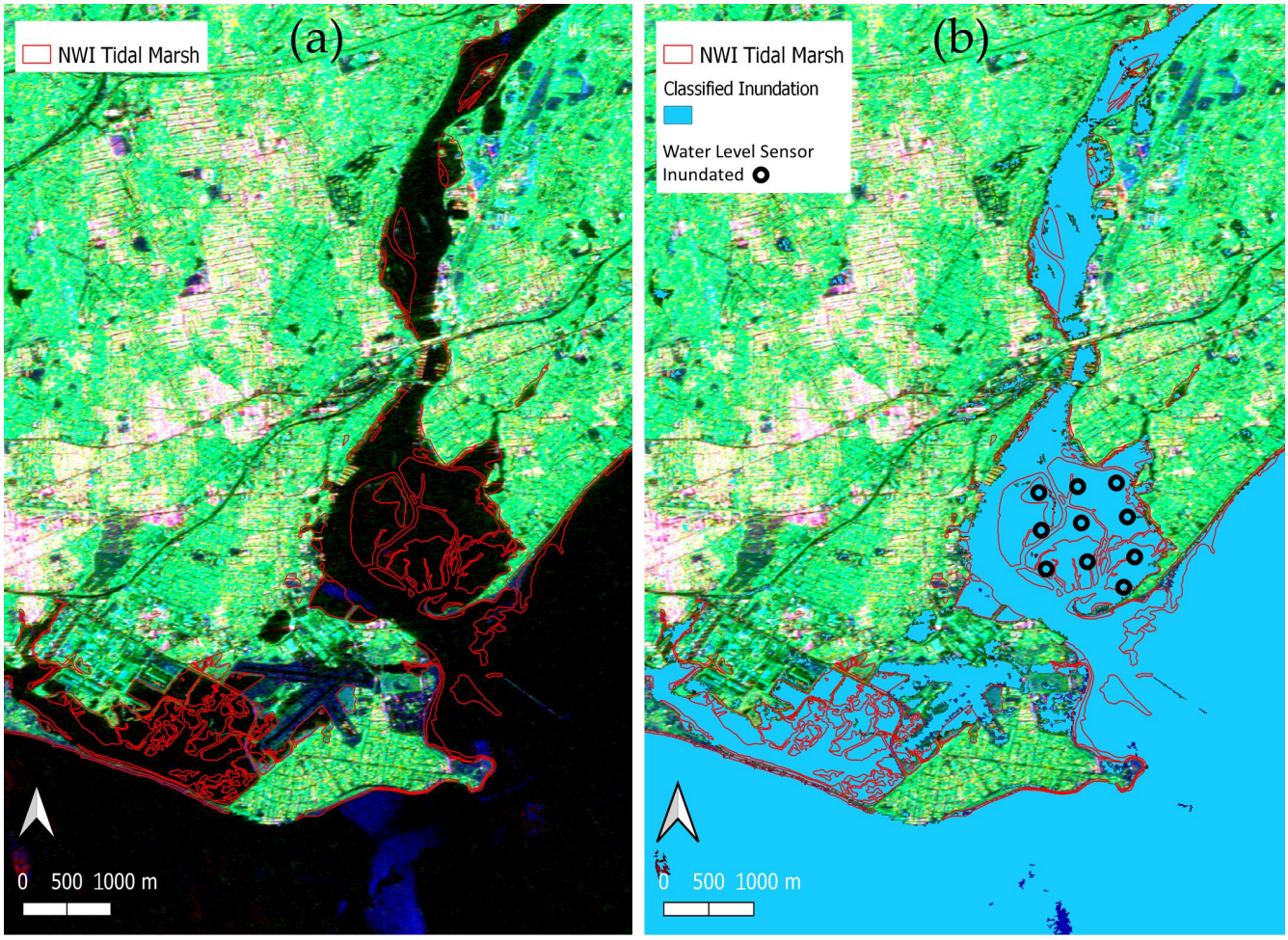

Figure 10. Wheeler Marsh high tide (2.582 m) PALSAR-2 image comparison between van Zyl polarimetric decomposition (**a**) and backscatter threshold-based inundation classification overlaid on the polarimetric decomposition (**b**). For the van Zyl decomposition, RGB channels correspond to double-bounce, volume, and surface scattering, respectively, with all channels scaled between −4 to −20 dB. All tidal marsh-dominated areas around Wheeler Marsh, including the Great Meadows system to the southwest and the Housatonic River wetlands to the north, were shown as inundated in the threshold-based classification. Water level sensor validation showed 10/10 sensor locations correctly classified as inundated.

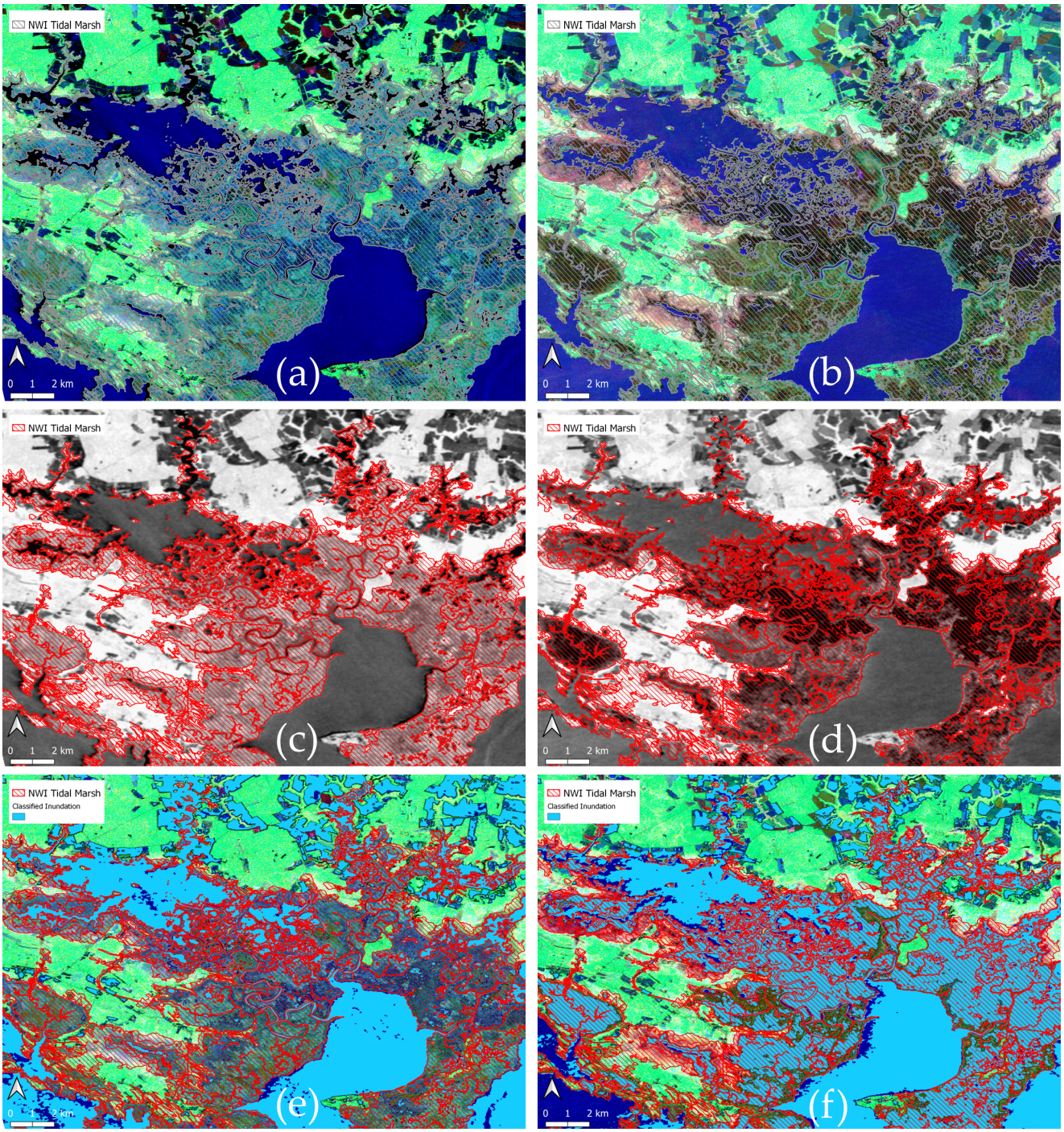

Figure 11. Comparison of PALSAR-2 imagery over Blackwater NWR for low tide (left panels) and high tide (right panels). Vertically descending panels correspond to van Zyl decomposition (**a,b**), HH backscatter (**c,d**), and backscatter-threshold classified inundation extent (**e,f**). van Zyl RGB channels correspond to double-bounce, volume scattering, and surface scattering, respectively. All SAR images scaled between −20 and −4 dB. Classified inundated area increases greatly when comparing the low tide classification (**e**) to the high tide classification (**f**) for NWI tidal marshes. In the van Zyl decompositions, surface scattering dominates at low tide (**a**) indicating a primary backscatter response from a rough moist soil surface. High tide (**b**) shows a decrease in total backscatter magnitude for all scattering types and a relative shift from surface scattering (cyan) to double-bounce (red and brown) with some volume scattering occurring in low tide and high tide images alike.

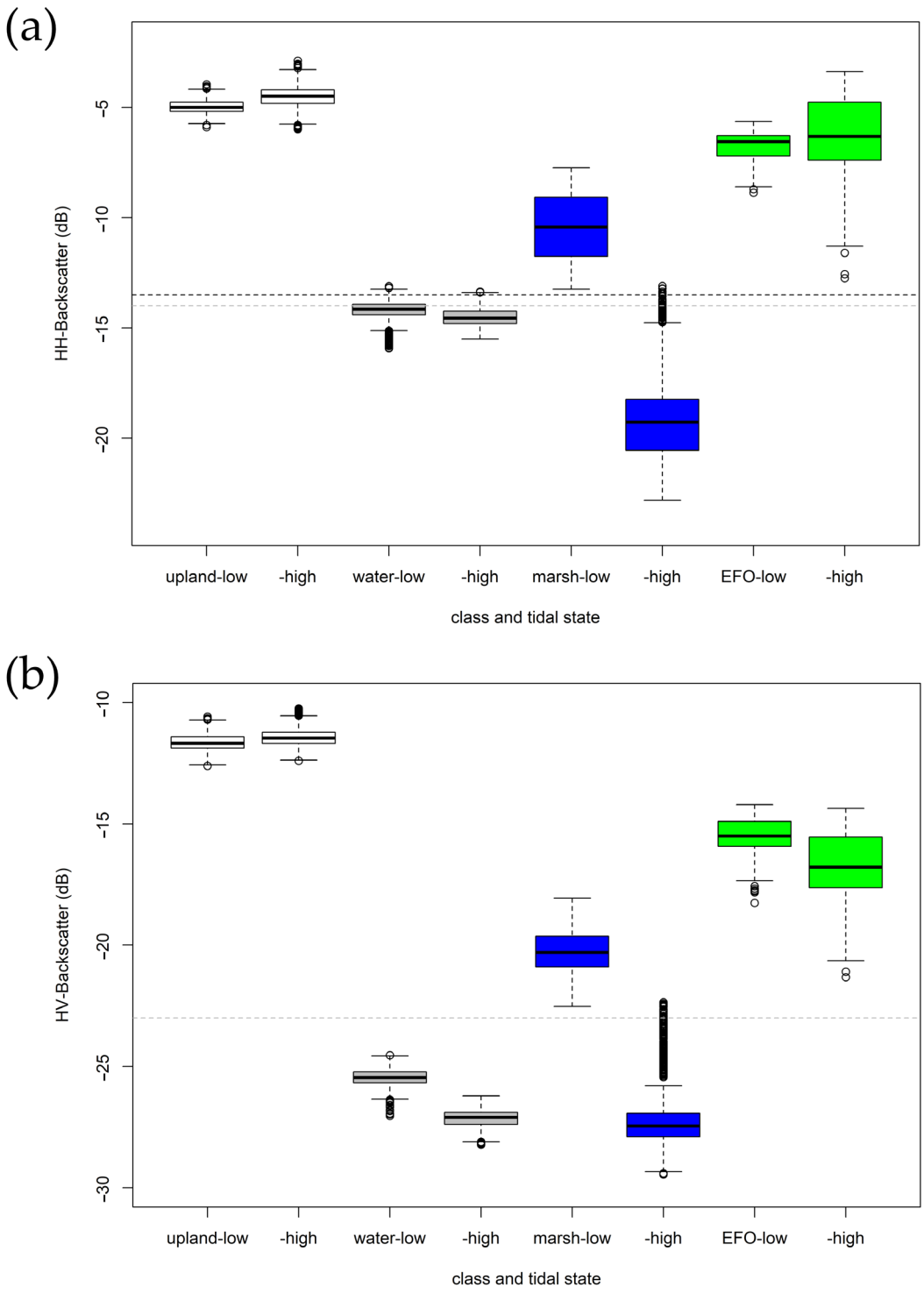

Figure 12. Blackwater NWR cover class PALSAR-2 backscatter distributions for HH (**a**) and HV (**b**) polarizations for low tide and tide images from Figure 11. These cover classes were previously established in Lamb et al. (2019) [45] from a combination of ground surveys and aerial imagery and include upland forest, open water, tidal marsh, and estuarine forested wetlands (EFO). For the HH polarization, a threshold of −13.5 dB established for PALSAR imagery in Lamb et al. (2019) [45] is depicted as a black dashed line. The classification thresholds established in this publication of −14 dB for HH and −23 dB for HV are depicted as grey lines indicating good consistency with the findings from Wheeler Marsh.

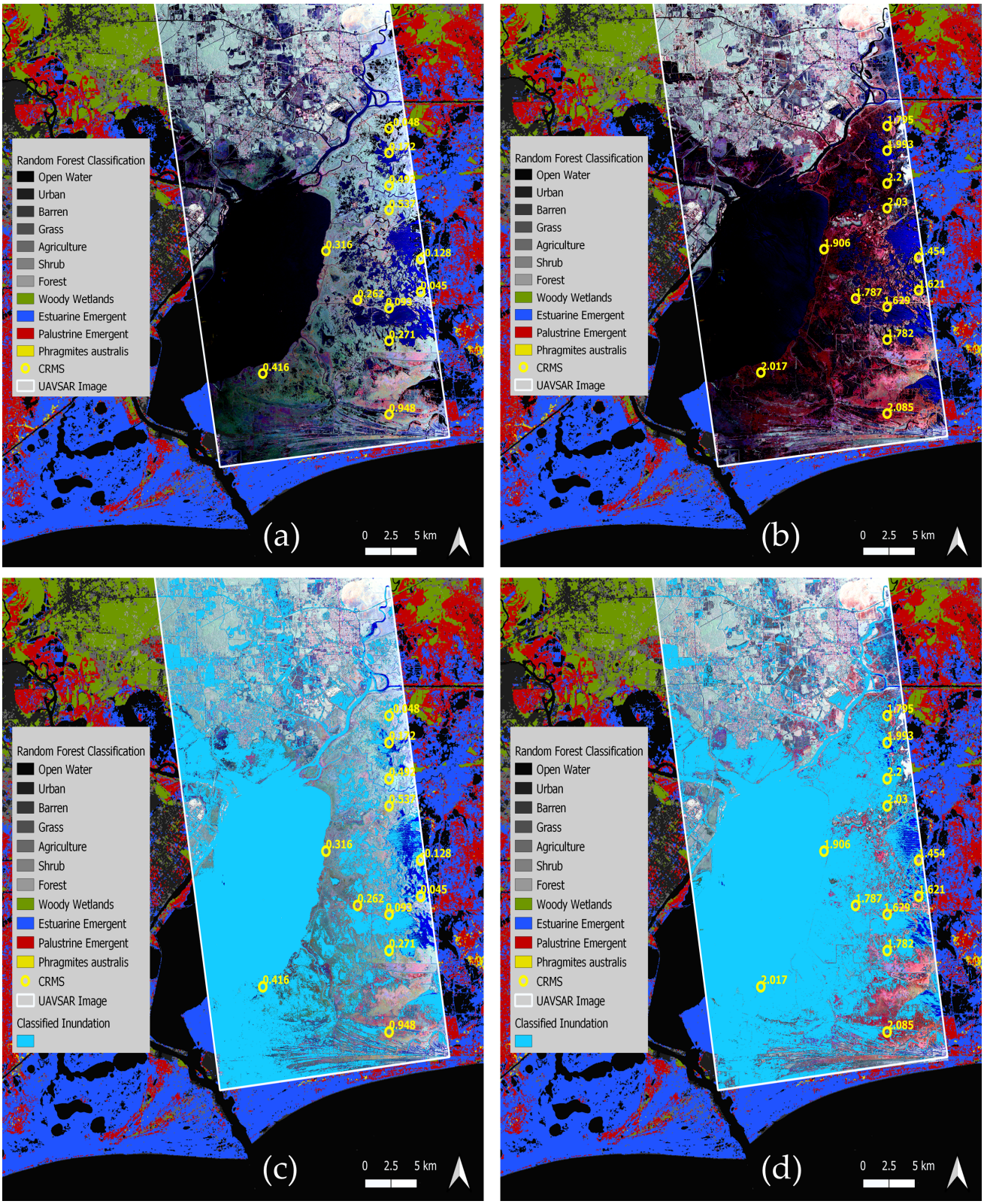

Figure 13. Sabine River low tide (panels (**a**,**c**)) and high tide (panels (**b**,**d**)) UAVSAR imagery obtained on 12 August 2019 (tidal stage 0.497 m) and 23 September 2019 (tidal stage 0.939 m), respectively, showing van Zyl decompositions (**a**,**b**) and overlaid backscatter-threshold inundation classifications (**c**,**d**). Decompositions scaled between −4 to −20 dB for surface scattering (blue) and double-bounce (red), −10 to −26 for volume scattering (green). The southern Sabine River region is dominated by both palustrine and estuarine marshes, as indicated by the random forest cover classification [46] expanding beyond the UAVSAR swath. CRMS water level values are expressed in feet.

The results from Wheeler Marsh, Blackwater NWR, and the Sabine River demonstrate that marsh inundation can be accurately classified with L-band SAR even when tidal range variations result in different scattering mechanisms between vegetation submergence (specular scattering) and partial submergence (double-bounce scattering).

4. Discussion

This study sought to develop and validate SAR inundation products while investigating factors influencing SAR scattering mechanisms in tidal marshes. Our results demonstrated that L-band SAR produces the most consistent characterization of tidal marsh inundation state. The comparison of L-band SAR (Figure 6), C-band SAR (Figure 5), and optical inundation products (Figure 4) over Wheeler Marsh, in conjunction with the correlation analysis in Table 2, demonstrates important differences between these sensor types. L-band backscatter had the highest correlations with tidal stage. This finding was consistent across different study sites, and for different NWI classes within these sites. For instance, Wheeler Marsh, Great Meadows, and Nissequogue River sites contained both NWI regularly flooded tidal marsh (E2EM1N) and NWI irregularly flooded tidal marsh (E2EM1P), with L-band backscatter being highly correlated with tidal stage ($R > 0.9$) in all cases. Optical indices (e.g., mNDWI) that formulate products like DWSE were also highly correlated with tidal stage for E2EM1N marshes shown in Table 2 but exhibited significant reductions in correlation for E2EM1P marshes that generally have denser vegetation. C-band SAR correlation with tidal stage was moderately high for the VH channel over sparsely vegetated wetlands, or for the VV/VH ratio for wetlands with relatively dense vegetation. This is illustrated in Table 2 for Wheeler Marsh E2EM1N marshes ($R = 0.875$) and Blackwater E2EM1N and E2EM1P marshes ($R = 0.889$, $R = 0.856$).

C-band inundation products derived from multi-date imagery with VH and VV/VH polarizations slightly underperformed relative to L-band inundation products derived using backscatter thresholding applied to individual scenes. However, the C-band inundation products yielded some important insights. For the highest tide C-band image (Figure 5d), the sparsely vegetated southern portion of Wheeler Marsh was primarily classified as inundated with the VH channel change detection, while the more densely vegetated northern portion of the marsh was classified as inundated with the VV/VH ratio change detection. This indicates that while C-band SAR imagery can be effective in assessment of tidal marsh inundation state, a priori knowledge of vegetation structure is much more critical for C-band imagery than L-band imagery. While C-band SAR may be less sensitive to sub-canopy inundation state than L-band, particularly for densely vegetated canopies, our results demonstrated that C-band VV/VH inundation products were classified with a reasonable accuracy of 76.4% for GCReW, far exceeding the accuracy of optical products.

MIMICS radiometric modeling further elucidated the findings of our image analyses, inundation product development, and validation with water level observations. The simulation of tidal inundation (i.e., wet soil transitioning to an inundated surface) revealed pronounced decreases in L-band backscatter compared to C-band backscatter, indicating that L-band signals have less interaction with emergent vegetation canopies. The differences in the polarimetric responses of C-band imagery were further explored with MIMICS demonstrating that simulated HH backscatter was more sensitive to changes in surface hydrologic state than VV backscatter at C-band wavelengths (Figure 8a vs. Figure 9a). This suggests that HH-polarized C-band signals tend to penetrate vertically structured emergent canopies to a greater degree than VV-polarized signals. L-band signals did not exhibit considerable differences between the VV and HH polarizations, both showing a pronounced decrease in backscatter in response to inundation of vegetated canopies. The decrease in total L-band backscatter is explained by significant reductions in surface

and volume scattering while phase-coherent double-bounce scattering remained present. The double-bounce scattering mechanism was nearly non-existent for C-band signals, particularly for the VV polarization. This finding has important implications for InSAR wetland water level studies where high coherence is a prerequisite for proper interferogram formation, and suggests that L-band imagery should be selected over C-band imagery when available, corroborating previous findings [64].

Our MIMICS radiometric modeling efforts were largely corroborated by polarimetric decompositions comparing low tide and high tide PALSAR-2 and UAVSAR scenes. High tide images showed consistent shifts to either double-bounce scattering in the case of partial submergence of vegetation or specular scattering (low total backscatter) in the case of complete vegetation submergence, both of which corresponded to increases in classified inundated area (Figures 10, 11 and 13). L-band threshold-classified inundation products were found to be 90% accurate over Wheeler Marsh (Figure 6) and 100% accurate for an additional high tide image over Wheeler Marsh (Figure 10). The fact this same thresholding approach (Equation (1)) could be applied outside of Wheeler Marsh and consistently matched areas shifting to double-bounce scattering during high tide presents further evidence of the utility of this approach. Additionally, our results show a largely accurate inundation classification for both open water and inundated marshes over Wheeler Marsh, Great Meadows, the Housatonic River, and the Long Island Sound estuary (Figure 10).

A notable limitation of this thresholding approach is the fact that both rough waters and open water/inundated wetlands imaged in the near range portion of a given SAR swath were at times misclassified as non-inundated (S3 & S4). This misclassification likely resulted from a rough water surface increasing co-polarized backscatter above the −14 dB threshold value. For example, HH-polarized imagery (Figure 12a) often exceeded threshold values compared to HV-polarized imagery (Figure 12b) for open water regions of the Blackwater NWR site. However, these limitations are expected to be less important for NISAR, as the near range angle is expected to be further off nadir than UAVSAR (32.0 vs. 25.0 degrees, respectively). Yet, this is a noteworthy limitation for inundation detection in cases like extreme flood monitoring where rough water surfaces my produce high co-polarized backscatter, indicating that thresholding of cross-polarized imagery (HV channel) may be most appropriate for rapid and accurate production of flood maps (Figure 12b).

While the findings of this study were informative and highlight the benefits of using single-date L-band imagery for classifying tidal marsh inundation, there are additional limitations to address. This study focused on a limited number of study sites and possible validation opportunities. Wheeler Marsh had the most comprehensive image record between L-band, C-band, and optical, but was limited to validation with 60 water level observations for L-band and 80 observations for C-band. Blackwater NWR had only two pairs of low tide and high tide images, and GCReW had no high tide L-band images, which prevented a comprehensive validation across these sites. The availability of L-band imagery is expected to increase with the PALSAR-2 ScanSAR record becoming public (https://www.eorc.jaxa.jp/ALOS/en/dataset/alos_open_and_free_e.htm) (accessed on 15 May 2024). Expanding algorithm evaluation and associated validations on these additional images may prove informative ahead of the launch of NISAR. For both Wheeler Marsh and GCReW, because calibrations with NOAA tide gauges were so accurate (R^2 >= 0.949) (S1), in-marsh water levels can be estimated for these sites with high accuracy for the record of the NOAA tide gauge observations in the future.

Another limitation, relevant to both the backscatter threshold classification approach and our MIMICS modeling effort, has to do with assumptions about surface roughness. In general, it was assumed that marsh soil had a fairly standard soil roughness [58] but the inundated (water) surface was modeled as a smooth surface. While sub-canopy inundation

does generally have a smooth surface due to attenuation of turbulent flows by stems, shielding of the water's surface from wind, and marshes being less impacted by waves than connected estuaries, the assumption of a water surface with no roughness is idealized. It is likely that the use of the smooth water surface increased the double-bounce scattering and decreased total scattering in our modeling efforts. Despite this limitation, the pronounced differences between C-band and L-band would not be expected to change substantially. Slightly different limitations in assumptions about surface roughness also appear in the classification of L-band imagery over Wheeler Marsh where southern portions of the marsh were incorrectly classified as inundated during low tide. These false detections of inundation are likely attributable to the presence of smooth mudflats in this area. When mudflats are sufficiently smooth, they will produce high specular (forward) scattering, and thus, low backscatter, meaning they may be incorrectly classified as inundated. Having an a priori classification of mudflats could help distinguish these regions from vegetated wetlands. Optical imagery may be more accurate in detecting mudflats and classifying the inundation state of mudflats than SAR, as optical indices and products can identify spectral reflectance changes indicating the presence of vegetation, soil, and water, and are less impacted by surface roughness variability than SAR. DSWE optical products demonstrated high performance in inundation detection for sparsely vegetated wetlands, mudflats and open water (Figure 4b). For these reasons, DSWE products should be further evaluated as a complement to SAR imagery when deriving inundation products.

A related area of assumption of this study that needs to be addressed pertains to soil moisture. Our radiometric modeling effort demonstrated that marsh soils with moisture values below 25% were erroneously classified as inundated due to low backscatter values (Figure 7). While this is a limitation that needs be documented, it is generally an uncommon occurrence in the hydric soils of tidal marshes. For instance, Moffett et al. (2010) [65] reported average soil volumetric moisture contents of 83% (*SD* = 15%) in San Francisco Bay tidal marshes, a value range well above 25%. C-band backscatter was not prone to this misclassification, likely due to decreased interaction with the surface relative to vegetation canopies when compared to L-band.

While our radiometric modeling efforts focused on a common range of marsh vegetation conditions, Bourgeau-Chavez et al. (2013) [66] demonstrated that *Phragmites australis* canopy heights reach up to 5 m and tend to exhibit SAR backscatter values substantially higher than other emergent species. Future research efforts could include a more comprehensive performance analysis over marsh sites dominated by higher biomass emergent vegetation and woody shrub marsh vegetation (e.g., *Spartina cynosuroides*, *Phragmites australis*, and *Iva frutescens*).

It is important to state that the backscatter threshold classification used in this study applies only to emergent wetland systems and is not suitable for mangroves and forested wetlands, which often exhibit increases in co-polarized backscatter intensity when inundated due to strongly enhanced double-bounce scattering, as shown in Figure 12a for the estuarine forested wetlands. For classification of inundation in woody wetlands, single image backscatter thresholding would need to be replaced with change detection approaches as described in the NISAR Science User's Handbook (pages 97–104) [44]. Single image thresholding and change detection approaches may be combined in rule-based classifications to establish separate retrievals of inundation state for different types of wetland vegetation (e.g., herbaceous vs. woody) and for different biomass categories. C-band SAR may prove quite effective to this end and has been demonstrated effective in differentiating emergent and forested wetlands based on multi-temporal backscatter signatures [45,46]. At the most general level, ancillary products accurately characterizing marsh extent are required to produce marsh inundation products. The European Space Agency's WorldCover

product mapping herbaceous (emergent) wetlands on a global scale at a 10 m resolution may be quite suitable to this end [67]. More nuanced and accurate inundation classification approaches may be developed by incorporating ancillary wetland biomass products like those produced by Byrd et al. (2018) [68]. While this wetland biomass product only covers coastal US sites, the dataset provides an opportunity for further testing of inundation classification algorithms over a range of biomass conditions. The applicability of our approaches to inland (non-tidal) marshes is expected to be quite high since the physically mediated L-band backscatter changes leveraged to map inundation are not unique to tidal settings.

5. Conclusions

We evaluated inundation-mediated changes in C-band and L-band SAR backscatter for tidal marsh systems. When tidal marshes inundate, L-band backscatter decreased substantially for the HH polarization, in both image analyses and radiometric modeling simulations. While C-band image analyses and radiometric simulations show backscatter responses to changes in inundation state, the responses varied in both direction and magnitude depending on SAR polarization, tidal stage, and vegetation structure. For these reasons, inundation classifications using C-band imagery required change detection approaches that incorporate multi-date imagery. For L-band imagery, HH and HV backscatter distributions were completely separable comparing low tide and high tide imagery enabling inundation product development with backscatter thresholding applied to single-date imagery. Our L-band backscatter threshold approach resulted in classification accuracies of 90% for a validation effort using water level sensors. These findings have significant implications for the upcoming NISAR mission as they suggest that simple thresholds applied to individual scenes produce marsh inundation products exceeding the 80% accuracy standard for NISAR science products. Radiometric modeling was critical to this effort as it elucidated changes in SAR scattering mechanisms in response to inundation. For L-band signals, inundation causes decreases in total backscatter, with double-bounce scattering making up a larger portion of total backscatter relative to surface and volume scattering. This finding was corroborated by image-based polarimetric decompositions and has significant implications for InSAR-based wetland studies focused on water level change estimates. For NISAR, the planned 12-day repeat interval is identical to Sentinel-1 C-band SAR offering short temporal baselines. However, NISAR's L-band frequency should provide far better InSAR coherence than C-band, and thus interferogram formation. Overall, this study suggests that L-band imagery will be a critical tool for tidal marsh observation in the future, and accurate classifications of inundation state can be achieved with simple thresholding approaches below certain biomass thresholds. Further improvements in inundation product accuracy could be achieved with the use of machine learning (ML) approaches. ML may provide higher performance in the estimation of tidal marsh inundation state and broader utility in classifying inundation for additional landcover classes adjacent to tidal marshes, as has been demonstrated by SAR flood mapping studies [69–71].

Supplementary Materials: The following supporting information can be downloaded at: https://www.mdpi.com/article/10.3390/rs17020263/s1.

Author Contributions: Conceptualization, B.T.L., K.C.M. and M.A.T.; methodology, B.T.L., K.C.M., M.A.T. and D.S.T.; software, B.T.L.; validation, B.T.L.; formal analysis, B.T.L.; investigation, B.T.L., K.C.M. and M.A.T.; resources, M.A.T., K.C.M. and B.T.L.; data curation, B.T.L.; writing—original draft preparation, B.T.L.; writing—review and editing, B.T.L., K.C.M., M.A.T. and D.S.T.; visualization, B.T.L.; supervision, M.A.T. and K.C.M.; project administration, M.A.T. and K.C.M.; funding acquisition, M.A.T., K.C.M. and B.T.L. All authors have read and agreed to the published version of the manuscript.

Funding: This research was funded by the NASA Earth and Space Science Fellowship Program (grant 80NSSC17K0365), the NASA Interdisciplinary Science Program (grant 80NSSC17K0258), the NASA Carbon Cycle Science Program (grant NNX14AP06G), the NASA Carbon Monitoring Systems Program (grant NNG23OB31A), and the NISAR Science Team (grant 80NSSC19K1513). Portions of this work were carried out at the Jet Propulsion Laboratory, California Institute of Technology, under contract to the National Aeronautics and Space Administration.

Data Availability Statement: Datasets and classification products from this study are available upon request by contacting the authors.

Acknowledgments: This research was conducted in part under the framework of the ALOS Kyoto and Carbon Initiative. This manuscript benefited greatly from suggestions by Dorothy Peteet of Lamont-Doherty Earth Observatory and Andrew Reinmann of the CUNY Advanced Science Research Center. We also thank Matt Whitbeck of USFWS for providing water level observations for the Blackwater NWR site.

Conflicts of Interest: The authors declare no conflicts of interest.

References

1. Fettrow, S.; Jeppi, V.; Wozniak, A.; Vargas, R.; Michael, H.; Seyfferth, A.L. Physiochemical Controls on the Horizontal Exchange of Blue Carbon Across the Salt Marsh-Tidal Channel Interface. *J. Geophys. Res. Biogeosci.* **2023**, *128*, e2023JG007404. [CrossRef]
2. Fichot, C.G.; Tzortziou, M.; Mannino, A. Remote sensing of dissolved organic carbon (DOC) stocks, fluxes and transformations along the land-ocean aquatic continuum: Advances, challenges, and opportunities. *Earth-Sci. Rev.* **2023**, *242*, 104446. [CrossRef]
3. Menendez, A.; Tzortziou, M.; Neale, P.; Megonigal, P.; Powers, L.; Schmitt-Kopplin, P.; Gonsior, M. Strong Dynamics in Tidal Marsh DOC Export in Response to Natural Cycles and Episodic Events From Continuous Monitoring. *J. Geophys. Res. Biogeosci.* **2022**, *127*, e2022JG006863. [CrossRef]
4. Glaser, C.; Frei, S.; Massmann, G.; Gilfedder, B.S. Tidal creeks as hot-spots for hydrological exchange in a coastal landscape. *J. Hydrol.* **2021**, *597*, 126158. [CrossRef]
5. Hopkinson, C.S.; Wolanski, E.; Cahoon, D.R.; Perillo, G.M.E.; Brinson, M.M. *Coastal Wetlands: A Synthesis*; Elsevier: Amsterdam, The Netherlands, 2018; ISBN 9780444638939.
6. Temmink, R.J.M.; Lamers, L.P.M.; Angelini, C.; Bouma, T.J.; Fritz, C.; Van de Koppel, J.; Lexmond, R.; Rietkerk, M.; Silliman, B.R.; Joosten, H.; et al. Recovering wetland biogeomorphic feedbacks to restore the world's biotic carbon hotspots. *Science* **2022**, *376*, eabn1479. [CrossRef] [PubMed]
7. Tzortziou, M.; Neale, P.J.; Osburn, C.L.; Megonigal, J.P.; Maie, N.; Jaffe, R. Tidal marshes as a source of optically and chemically distinctive colored dissolved organic matter in the Chesapeake Bay. *Limnol. Oceanogr.* **2008**, *53*, 148–159. [CrossRef]
8. Kirwan, M.L.; Temmerman, S.; Skeehan, E.E.; Guntenspergen, G.R.; Fagherazzi, S. Overestimation of marsh vulnerability to sea level rise. *Nat. Clim. Chang.* **2016**, *6*, 253–260. [CrossRef]
9. Dahl, K.A.; Fitzpatrick, M.F.; Spanger-Siegfried, E. Sea level rise drives increased tidal flooding frequency at tide gauges along the U.S. East and Gulf Coasts: Projections for 2030 and 2045. *PLoS ONE* **2017**, *12*, e0170949. [CrossRef]
10. Ganju, N.K.; Defne, Z.; Kirwan, M.L.; Fagherazzi, S.; D'Alpaos, A.; Carniello, L. Spatially integrative metrics reveal hidden vulnerability of microtidal salt marshes. *Nat. Commun.* **2017**, *8*, 14156. [CrossRef]
11. McFeeters, S.K. Using the normalized difference water index (ndwi) within a geographic information system to detect swimming pools for mosquito abatement: A practical approach. *Remote Sens.* **2013**, *5*, 3544–3561. [CrossRef]
12. Du, Y.; Zhang, Y.; Ling, F.; Wang, Q.; Li, W.; Li, X. Water bodies' mapping from Sentinel-2 imagery with Modified Normalized Difference Water Index at 10-m spatial resolution produced by sharpening the swir band. *Remote Sens.* **2016**, *8*, 354. [CrossRef]
13. Sun, D.; Yang, T.; Li, S.; Goldberg, M.; Kalluri, S.; Helfrich, S.; Sjonberg, B.; Zhou, L.; Zhang, Q.; Straka, W.; et al. Hazard or Non-Hazard Flood: Post Analysis for Paddy Rice, Wetland, and Other Potential Non-Hazard Flood Extraction from the VIIRS Flood Products. *ISPRS J. Photogramm. Remote Sens.* **2024**, *209*, 415–431. [CrossRef]
14. Pekel, J.-F.; Cottam, A.; Gorelick, N.; Belward, A.S. High-resolution mapping of global surface water and its long-term changes. *Nature* **2016**, *540*, 418–422. [CrossRef]
15. Jones, J.W. Improved automated detection of subpixel-scale inundation-revised Dynamic Surface Water Extent (DSWE) partial surface water tests. *Remote Sens.* **2019**, *11*, 374. [CrossRef]
16. Melack, J.M.; Hess, L.L. Areal extent of vegetative cover: A challenge to regional upscaling of methane emissions. *Aquat. Bot.* **2023**, *184*, 103592. [CrossRef]
17. Melnychenko, T.; Solovey, T. Mapping Water Bodies and Wetlands from Multispectral and SAR Data for the Cross-Border River Basins of the Polish–Ukrainian Border. *Water* **2024**, *16*, 407. [CrossRef]

18. Ottinger, M.; Kuenzer, C. Spaceborne L-Band synthetic Aperture Radar Data for geoscientific analyses in coastal land applications: A review. *Remote Sens.* **2020**, *12*, 2228. [CrossRef]
19. Pope, K.O.; Rejmankova, E.; Paris, J.F.; Woodruff, R. Detecting Seasonal Cycle of the Yucatan Peninsula with SIR-C Polarmetric Radar Imagery. *Remote Sens. Environ.* **1997**, *59*, 157–166. [CrossRef]
20. Kasischke, E.S.; Smith, K.B.; Bourgeau-Chavez, L.L.; Romanowicz, E.A.; Brunzell, S.; Richardson, C.J. Effects of seasonal hydrologic patterns in south Florida wetlands on radar backscatter measured from ERS-2 SAR imagery. *Remote Sens. Environ.* **2003**, *88*, 423–441. [CrossRef]
21. Lang, M.W.; Kasischke, E.S. Using C-band synthetic aperture radar data to monitor forested wetland hydrology in Maryland's coastal plain, USA. *IEEE Trans. Geosci. Remote Sens.* **2008**, *46*, 535–546. [CrossRef]
22. Hong, S.H.; Wdowinski, S. Double-bounce component in cross-polarimetric SAR from a new scattering target decomposition. *IEEE Trans. Geosci. Remote Sens.* **2014**, *52*, 3039–3051. [CrossRef]
23. Schmitt, A.; Brisco, B. Wetland Monitoring Using the Curvelet-Based Change Detection Method on Polarimetric SAR Imagery. *Water* **2013**, *5*, 1036–1051. [CrossRef]
24. Kim, J.-W.; Lu, Z.; Jones, J.W.; Shum, C.K.; Lee, H.; Jia, Y. Monitoring Everglades freshwater marsh water level using L-band synthetic aperture radar backscatter. *Remote Sens. Environ.* **2014**, *150*, 66–81. [CrossRef]
25. Moser, L.; Schmitt, A.; Wendleder, A.; Roth, A. Monitoring of the Lac Bam wetland extent using dual-polarized X-band SAR data. *Remote Sens.* **2016**, *8*, 302. [CrossRef]
26. Brisco, B.; Ahern, F.; Murnaghan, K.; White, L.; Canisus, F.; Lancaster, P. Seasonal change in wetland coherence as an aid to wetland monitoring. *Remote Sens.* **2017**, *9*, 158. [CrossRef]
27. Jensen, K.; McDonald, K.; Podest, E.; Rodriguez-Alvarez, N.; Horna, V.; Steiner, N. Assessing L-Band GNSS-reflectometry and imaging radar for detecting sub-canopy inundation dynamics in a tropical wetlands complex. *Remote Sens.* **2018**, *10*, 1431. [CrossRef]
28. Rosenqvist, J.; Rosenqvist, A.; Jensen, K.; McDonald, K. Mapping of maximum and minimum inundation extents in the amazon basin 2014–2017 with ALOS-2 PALSAR-2 scan SAR time-series data. *Remote Sens.* **2020**, *12*, 1326. [CrossRef]
29. Shen, X.; Wang, D.; Mao, K.; Anagnostou, E.; Hong, Y. Inundation extent mapping by synthetic aperture radar: A review. *Remote Sens.* **2019**, *11*, 879. [CrossRef]
30. Surampudi, S.; Kumar, V. Hybrid Naïve Bayes Gaussian mixture models and SAR polarimetry based automatic flooded vegetation studies using PALSAR-2 data. *Remote Sens. Appl. Soc. Environ.* **2024**, *36*, 101361. [CrossRef]
31. Salem, A.; Hashemi-Beni, L. Inundated Vegetation Mapping Using SAR Data: A Comparison of Polarization Configurations of UAVSAR L-Band and Sentinel C-Band. *Remote Sens.* **2022**, *14*, 6374. [CrossRef]
32. Oakes, G.; Hardy, A.; Bunting, P.; Rosenqvist, A. RadWet-L: A Novel Approach for Mapping of Inundation Dynamics of Forested Wetlands Using ALOS-2 PALSAR-2 L-Band Radar Imagery. *Remote Sens.* **2024**, *16*, 2078. [CrossRef]
33. Huang, C.; Smith, L.C.; Kyzivat, E.D.; Fayne, J.V.; Ming, Y.; Spence, C. Tracking transient boreal wetland inundation with Sentinel-1 SAR: Peace-Athabasca Delta, Alberta and Yukon Flats, Alaska. *GISci. Remote Sens.* **2022**, *59*, 1767–1792. [CrossRef]
34. Ramsey, E.; Werle, D.; Suzuoki, Y.; Rangoonwala, A.; Lu, Z. Limitations and Potential of Satellite Imagery to Monitor Environmental Response to Coastal Flooding. *J. Coast. Res.* **2012**, *280*, 457–476. [CrossRef]
35. Ramsey, E.; Rangoonwala, A.; Bannister, T. Coastal Flood Inundation Monitoring with Satellite C-band and L-band Synthetic Aperture Radar Data. *J. Am. Water Resour. Assoc.* **2013**, *49*, 1239–1260. [CrossRef]
36. Zhang, M.; Li, Z.; Tian, B.; Zhou, J.; Zeng, J. A method for monitoring hydrological conditions beneath herbaceous wetlands using multi-temporal ALOS PALSAR coherence data. *Remote Sens. Lett.* **2015**, *6*, 618–627. [CrossRef]
37. San Martín, L.; Morandeira, N.S.; Grimson, R.; Rajngewerc, M.; González, E.B.; Kandus, P. The contribution of ALOS/PALSAR-1 multi-temporal data to map permanently and temporarily flooded coastal wetlands. *Int. J. Remote Sens.* **2020**, *41*, 1582–1602. [CrossRef]
38. Liao, T.H.; Simard, M.; Denbina, M.; Lamb, M.P. Monitoring water level change and seasonal vegetation change in the coastal wetlands of louisiana using L-band time-series. *Remote Sens.* **2020**, *12*, 2351. [CrossRef]
39. Zhang, X.; Jones, C.E.; Simard, M.; Passalacqua, P.; Oliver-Cabrera, T.; Fagherazzi, S. Vegetation promotes flow retardation and retention in deltaic wetlands. *Limnol. Oceanogr. Lett.* **2024**, *9*, 644–652. [CrossRef]
40. Atwood, D.; Battaglia, M.; Bourgeau-Chavez, L.; Ahern, F.; Murnaghan, K.; Brisco, B. Exploring Polarimetric Phase of Microwave Backscatter from Typha Wetlands. *Can. J. Remote Sens.* **2020**, *46*, 49–66. [CrossRef]
41. Tanis, F.J.; Bourgeau-Chavez, L.L.; Dobson, M.C. Application of ERS-1 SAR for coastal inundation. *Proc. IGARSS '94-1994 IEEE Int. Geosci. Remote Sens. Symp.* **1994**, *3*, 1481–1483.
42. Kasischke, E.S.; Bourgeau-Chavez, L.L. Monitoring south Florida wetlands using ERS-1 SAR imagery. *Photogramm. Eng. Remote Sens.* **1997**, *63*, 281–291.
43. Slatton, K.C.; Crawford, M.M.; Chang, L. Modeling temporal variations in multipolarized radar scattering from intertidal coastal wetlands. *ISPRS J. Photogramm. Remote. Sens.* **2008**, *63*, 559–577. [CrossRef]

44. NISAR Science Team; Simard, M. *NASA-ISRO SAR (NISAR) Mission Science Users' Handbook*; California Institute of Technology, Jet Propulsion Laboratory: Pasadena, CA, USA, 2018.
45. Lamb, B.T.; Tzortziou, M.A.; McDonald, K.C. Evaluation of approaches for mapping tidal wetlands of the Chesapeake and Delaware Bays. *Remote Sens.* **2019**, *11*, 2366. [CrossRef]
46. Lamb, B.T.; Tzortziou, M.A.; McDonald, K.C. A fused radar-optical approach for mapping wetlands and deepwaters of the mid-atlantic and gulf coast regions of the United States. *Remote Sens.* **2021**, *13*, 2495. [CrossRef]
47. Nelson, N.G.; Munoz-Carpena, R.; Neale, P.J.; Tzortziou, M.; Megonigal, P.J. Temporal variability in the importance of hydrologic, biotic, and climatic descriptors of dissolved oxygen dynamics in a shallow tidal marsh creek. *Water Resour. Res.* **2017**, *53*, 5974–5997. [CrossRef]
48. Allen, A.L.; Gill, S.K. Tidal Characteristics of Blackwater National Wildlife Refuge. In *NOAA & USACE Technical Report*; NOAA Center for Operational Oceanographic Products and Services: Silver Spring, MD, USA, 2003.
49. McDonald, K.C.; Dobson, M.C.; Ulaby, F.T. Modeling multi-frequency diurnal backscatter from a walnut orchard. *Dig. Int. Geosci. Remote Sens. Symp.* **1991**, *3*, 1125–1128.
50. McDonald, K.C. Modeling Microwave Backscatter from Tree Canopies. Ph.D. Thesis, University of Michigan, Ann Arbor, MI, USA, 1991.
51. Farrell, J.M.; Murry, B.A.; Leopold, D.J.; Halpern, A.; Rippke, M.B.; Godwin, K.S.; Hafner, S.D. Water-level regulation and coastal wetland vegetation in the upper St. Lawrence River: Inferences from historical aerial imagery, seed banks, and Typha dynamics. *Hydrobiologia* **2010**, *647*, 127–144. [CrossRef]
52. Legault, R.; Zogg, G.P.; Travis, S.E. Competitive interactions between native Spartina alterniflora and non-native Phragmites australis depend on nutrient loading and temperature. *PLoS ONE* **2018**, *13*, e0192234. [CrossRef]
53. Ornes, W.; Kaplan, D. Macronutrient status of tall and short forms of Spartina alterniflora in a South Carolina salt marsh. *Mar. Ecol. Prog. Ser.* **1989**, *55*, 63–72. [CrossRef]
54. Tulbure, M.G.; Ghioca-Robrecht, D.M.; Johnston, C.A.; Whigham, D.F. Inventory and Ventilation Efficiency of Nonnative and Native Phragmites australis (Common Reed) in Tidal Wetlands of the Chesapeake Bay. *Estuaries Coasts* **2012**, *35*, 1353–1359. [CrossRef]
55. Uddin, M.N.; Robinson, R.W. Responses of plant species diversity, soil physical-chemical-microbial properties to Phragmites australis invasion along a density gradient. *Sci. Rep.* **2017**, *7*, 11007. [CrossRef] [PubMed]
56. Pokorny, M.; Orloff, N.; Mangold, J. Invasive Species Technical Note: Ecology and Management of Phragmites (*Phragmites australis* ssp. australis). In *USDA-NRCS Technical Note-Invasive Species—MT-35*; United States Department of Agriculture: Washington, DC, USA, 2017; pp. 1–13.
57. Materne, M.; Bush, T.; Houck, M.; Snell, S. Plant Guide for smooth cordgrass (*Spartina alterniflora*). In *USDA-Natural Resources Conservation Service*; Louisiana State Office: Baton Rouge, LA, USA, 2022.
58. Duan, X.; Jones, C.E. Coherent Microwave Scattering Model of Marsh Grass. *Radio Sci.* **2017**, *52*, 1578–1595. [CrossRef]
59. Hong, S.-H.; Kim, H.-O.; Wdowinski, S.; Feliciano, E. Evaluation of Polarimetric SAR Decomposition for Classifying Wetland Vegetation Types. *Remote Sens.* **2015**, *7*, 8563–8585. [CrossRef]
60. Varghese, A.O.; Suryavanshi, A.; Joshi, A.K. Analysis of different polarimetric target decomposition methods in forest density classification using C band SAR data. *Int. J. Remote Sens.* **2016**, *37*, 694–709. [CrossRef]
61. Van Zyl, J.J. Unsupervised classification of scattering behavior using radar polarimetry data. *IEEE Trans. Geosci. Remote Sens.* **1989**, *27*, 36–45. [CrossRef]
62. Ji, K.; Wu, Y. Scattering mechanism extraction by a modified Cloude-Pottier decomposition for dual polarization SAR. *Remote Sens.* **2015**, *7*, 7447–7470. [CrossRef]
63. Lamb, B. Tidal Wetland Inundation and Vegetation Phenology from Space: A Synthesis of Approaches for Characterizing Ecological Status and Inundation Dynamics in Tidal Wetlands with Remote Sensing Observations. Ph.D. Thesis, City University of New York, New York, NY, USA, 2020.
64. Oliver-Cabrera, T.; Wdowinski, S. InSAR-based mapping of tidal inundation extent and amplitude in Louisiana coastal wetlands. *Remote Sens.* **2016**, *8*, 393. [CrossRef]
65. Moffett, K.B.; Robinson, D.A.; Gorelick, S.M. Relationship of Salt Marsh Vegetation Zonation to Spatial Patterns in Soil Moisture, Salinity, and Topography. *Ecosystems* **2010**, *13*, 1287–1302. [CrossRef]
66. Bourgeau-Chavez, L.L.; Kowalski, K.P.; Carlson, M.L.; Scarbrough, K.A.; Powell, R.B.; Brooks, C.N.; Huberty, B.; Jenkins, L.K.; Banda, E.C.; Galbraith, D.M.; et al. Mapping invasive Phragmites australis in the coastal Great Lakes with ALOS PALSAR satellite imagery for decision support. *J. Great Lakes Res.* **2013**, *39*, 65–77. [CrossRef]
67. Zanaga, D.; Van De Kerchove, R.; Daems, D.; De Keersmaecker, W.; Brockmann, C.; Kirches, G.; Wevers, J.; Cartus, O.; Santoro, M.; Fritz, S.; et al. *ESA WorldCover 10 m 2021 v200*; European Space Agency: Paris, France, 2022.

68. Byrd, K.B.; Ballanti, L.; Thomas, N.; Nguyen, D.; Holmquist, J.R.; Simard, M.; Windham-Myers, L. A remote sensing-based model of tidal marsh aboveground carbon stocks for the conterminous United States. *ISPRS J. Photogramm. Remote Sens.* **2018**, *139*, 255–271. [CrossRef]
69. Jiang, X.; Liang, S.; He, X.; Ziegler, A.D.; Lin, P.; Pan, M.; Wang, D.; Zou, J.; Hao, D.; Mao, G.; et al. Rapid and large-scale mapping of flood inundation via integrating spaceborne synthetic aperture radar imagery with unsupervised deep learning. *ISPRS J. Photogramm. Remote Sens.* **2021**, *178*, 36–50. [CrossRef]
70. Schumann, G.; Di Baldassarre, G.; Bates, P.D. The utility of spaceborne radar to render flood inundation maps based on multialgorithm ensembles. *IEEE Trans. Geosci. Remote Sens.* **2009**, *47*, 2801–2807. [CrossRef]
71. Wang, C.; Pavelsky, T.M.; Yao, F.; Yang, X.; Zhang, S.; Chapman, B.; Song, C.; Sebastian, A.; Frizzelle, B.; Frankenberg, E.; et al. Flood Extent Mapping During Hurricane Florence With Repeat-Pass L-Band UAVSAR Images. *Water Resour. Res.* **2022**, *58*, e2021WR030606. [CrossRef]